

# Interpreting the Role of the Magnetic Field from Dust Polarization Maps

Patrick M. Koch<sup>1</sup>, Ya-Wen Tang<sup>2,3,1</sup>, and Paul T. P. Ho<sup>1,4</sup>

pmkoch@asiaa.sinica.edu.tw

## ABSTRACT

Dust polarization observations from the Submillimeter Array (SMA) and the Caltech Submillimeter Observatory (CSO) are analyzed with the goal of providing a general tool to interpret the role of the magnetic field in molecular clouds. Magnetic field and dust emission gradient orientations are observed to show distinct patterns and features. The angle  $\delta$  between these two orientations can be interpreted as a magnetic field alignment deviation, assuming the emission gradient orientation to coincide with the density gradient orientation in the magnetohydrodynamics (MHD) force equation. In SMA high-resolution (collapsing) cores, additional symmetry properties in  $\delta$  can reveal accretion and outflow zones. All these observational findings suggest the angle  $\delta$  to be a relevant quantity that can assess the role of the magnetic field. Indeed, when comparing this angle with the (projection-free) magnetic field significance  $\Sigma_B$  (Koch, Tang & Ho 2012a), it is demonstrated that  $|\delta|$  yields an approximation to the change in  $\Sigma_B$ . Thus, changes in the magnetic field alignment deviation  $\delta$  trace changes in the role of the magnetic field. The angle  $\delta$  is observationally straightforward to determine, providing a tool to distinguish between zones of minor or significant magnetic field impact. This is exemplified by the CSO M+0.25+0.01, Mon R2, CO+0.02–0.02, M–0.02–0.07 sources and by the SMA high-resolution data from W51 e2, W51 North, Orion BN/KL and g5.89. Additional CSO sources are analyzed, providing further support of this result. Finally, based on the different features found in our sample of 31 sources in total, covering sizes from large-scale complexes to collapsing cores, a schematic evolutionary scenario is proposed. Here, the significance of the magnetic field evolves both with position and scale, and can be assessed with the angle  $\delta$ .

---

<sup>1</sup>Academia Sinica, Institute of Astronomy and Astrophysics, Taipei, Taiwan

<sup>2</sup>Université de Bordeaux, Observatoire Aquitain des Sciences de l'Univers, 2 rue de l'Observatoire, BP 89, F-33271 Floirac Cedex, France

<sup>3</sup>CNRS, UMR 5804, Laboratoire d'Astrophysique de Bordeaux, 2 rue de l'Observatoire, BP 89, F-33271 Floirac Cedex, France

<sup>4</sup>Harvard-Smithsonian Center for Astrophysics, 60 Garden Street, Cambridge, MA 02138, USA

*Subject headings:* ISM: clouds — ISM: magnetic fields, polarization — ISM: individual (W51 e2, W51 North, Orion BN/KL, G5.89-0.39, M+0.25+0.01, Mon R2, CO+0.02–0.02, M–0.02–0.07) — Methods: polarization

## 1. Introduction

Magnetic field observations toward star forming regions are becoming increasingly more important as the relevance of the magnetic field in the star formation process is being recognized in the literature (e.g., Crutcher 2012). On the observational side, recent instrumentation progress with improved sensitivities and polarization capabilities is advancing this field. Common observing techniques leading to some magnetic field information include Zeeman splitting, dust polarization, molecular line polarization and synchrotron emission. Any of these techniques has shortcomings and advantages, usually revealing only partial information of a magnetic field structure with its morphology, direction and strength. Zeeman splitting in spectral lines (e.g., Crutcher et al. 2009) typically leads to a line-of-sight field strength. In most cases, isolated positions or patches in a molecular cloud are mapped with this technique. Capturing the field morphology over a more extended area has been challenging. Recent observations of Zeeman splitting in masers are now able to start to trace the field morphology with a largely increased number of detections (Surcis et al. 2011; Vlemmings et al. 2011). Furthermore, results by Etoka et al. (2012) and Surcis et al. (2012) are consistently complementing dust polarization observations. In this latter technique, dust grains are expected to be aligned with their shorter axis parallel to the magnetic field lines most likely due to radiative torques (Draine & Weingartner 1996, 1997; Lazarian 2007), therefore revealing a plane-of-sky projected field orientation and morphology (e.g., Hildebrand 1988). A growing number of observations by both single dish telescopes (CSO, e.g., Kirby (2009); Dotson et al. (2010); Shinnaga et al. (2012), the James Clerk Maxwell Telescope (JCMT), e.g., Matthews et al. (2009)) and interferometers (the Berkeley-Illinois-Maryland Association (BIMA) array, e.g., Lai et al. (2002), the SMA, e.g., Girart et al. (2006); Tang et al. (2009b); Rao et al. (2009) and the Combined Array for Research in Millimeter-wave Astronomy (CARMA), Hull et al. (2013); Stephens et al. (2013)), in the (sub-)millimeter regime with resolutions from  $\sim 10''$  to sub-arcsecond, are detecting dust polarized emission showing systematic magnetic field structures. Additionally, a comparison of dust polarization observations at different frequencies can possibly also shed light on the nature of different grain populations (Vaillancourt et al. 2008; Vaillancourt & Matthews 2012). Complementary to dust polarization, linearly polarized spectral lines (Goldreich & Kylafis 1981, 1982) can probe the field morphology throughout the circumstellar envelope. Recent detections in various molecular lines are giving hints of a complex field structure in the envelope (Vlemmings et al.

2012; Girart et al. 2012). Unfortunately, both polarized line and dust emission do not provide information on the magnetic field strength. Additional modeling is needed. Recent techniques revealing additional magnetic field properties include e.g., polarization angle dispersion functions providing an estimate of the turbulent to mean magnetic field strength ratio (Hildebrand et al. 2009; Houde et al. 2009, 2011), comparison between co-existing ion and molecular line spectra constraining the ambipolar diffusion scale (Hezareh et al. 2011; Li & Houde 2008) and the polarization-intensity gradient method leading to a position-dependent estimate of the magnetic field strength (Koch, Tang & Ho 2012a,b). Finally, observing polarized synchrotron emission from relativistic electrons has the potential to map morphology and field strength in outflows and jets (Carrasco-González et al. 2010). This technique can, thus, ideally complement other magnetic field observations that are limited to core regions.

Dust polarization observations are probably providing the largest data sets so far to study the role of the magnetic field in star formation regions. In particular, these observations typically show a fairly large coverage, with polarized emission found throughout a significant area overlapping with Stokes  $I$  emission. Consequently, dust polarization maps are ideal to investigate systematic magnetic field features. Nevertheless, assessing the role of the magnetic field from such observations remains challenging. When interpreting the data, one is often left with either relying on theoretical concepts or comparing the data with numerical simulations (e.g., Padovani et al. 2012). In this work we aim at filling this gap. We propose a phenomenological approach. Based on systematically observed features we aim at providing guidelines for an interpretation of the role of the magnetic field. A particular emphasis is given to the relative importance of magnetic field versus gravity. To that purpose, the relation between the magnetic field and emission gradient orientation (the angle  $\delta$ ) – originally pointed out in Koch, Tang & Ho (2012a) – is studied here on a broader sample with a further expanded complementary analysis. We note that during the revision of this work, first numerical simulations analyzing the relative orientations of magnetic fields with respect to density structures were presented in Soler et al. (2013). Their results indicate that both density and the level of magnetization leave their imprints on the distributions of relative orientations.

This present work has benefited from a growing number of polarization observations over the past years. In particular, the high-resolution (sub-)arcsecond observations by the SMA (Tang et al. 2013, 2010, 2009b,a; Chen et al. 2012; Girart et al. 2013, 2009, 2006; Alves et al. 2010; Rao et al. 2009) were pioneering insights, methods and interpretation of the magnetic field that we are now also able to apply to earlier lower-resolution observations by other instruments. The proposed interpretation here is, thus, generally applicable to dust polarization observations. This study is part of the program on the SMA<sup>1</sup> (Ho, Moran & Lo 2004) to investigate the structure of the magnetic

---

<sup>1</sup> The Submillimeter Array is a joint project between the Smithsonian Astrophysical Observatory and the Academia Sinica Institute of Astronomy and Astrophysics, and is funded by the Smithsonian Institution and the Academia Sinica.

field from large to small scales.

The paper is organized as follows. In Section 2 we present observational results of the angle  $\delta$  from 2 different instruments, from  $\sim 20''$  to sub-arcsecond resolutions. We, additionally, provide an interpretation of the angle  $\delta$  by manipulating the MHD force equation. Supplementary material putting this in a context with our previous work is given in Appendix A. A brief summary and comparison of the relevant magnetic field quantities from our previous and current study follows in Section 3. Section 4 establishes the angle  $\delta$  as an approximation and reliable tracer for the changing role of the magnetic field over an observed map. Appendix B contains maps of a large sample in support of this finding. As a consequence, in Section 5 we propose a schematic scenario where the magnetic field significance evolves and is revealed through distinct changes and features in the angle  $\delta$ . Conclusion and summary are given in Section 6.

## 2. Intensity Gradient and Magnetic Field Orientations: the Angle $\delta$

Projected magnetic field orientations (rotated by  $90^\circ$  with respect to detected dust polarization orientations) form an angle  $\delta$  with their Stokes  $I$  dust intensity gradient orientations (Figure 1). Observationally, this angle  $\delta$  is straight forward to determine. Based on our recent results that point toward a connection in these orientations (Koch, Tang & Ho 2012a,b), we further investigate this finding here on a larger and diverse data set. The data analyzed in Section 2.1 and Appendix B with their systematic patterns in the angle  $\delta$  are suggestive for a direct physical meaning of this angle. A first intuitive interpretation of  $\delta$  was attempted in the context of the polarization - intensity gradient method (Koch, Tang & Ho 2012a). In this new method it was assumed that the emission intensity gradient is a measure for the result of all the forces acting in a molecular cloud. In Section 2.2 we will proceed to explain the angle  $\delta$  in the framework of ideal magneto-hydrodynamics (MHD). Appendix A discusses in detail how this interpretation is linked to the approach in Koch, Tang & Ho (2012a).

### 2.1. The Angle $\delta$ from Observations

We present results for the angle  $\delta$ , derived from both single dish and interferometric observations. In a first section we investigate features in  $\delta$  in 4 sources where the magnetic field is probed at different physical scales. As we will argue later in the Sections 4 and 5, we consider these sources as representative for different evolutionary stages in the star formation process, where the role of the magnetic field can be assessed by analyzing the angle  $\delta$ . In support of this argument, an additional set of 24 sources is analyzed in Appendix B. In the second section here, we then

focus on higher resolution observations which are probing systems with collapsing cores, where the angle  $\delta$  yet shows additional characteristics.

### 2.1.1. $|\delta|$ over Different Scales

Both Hertz on the CSO and SCUPOL on the JCMT have published catalogs of polarization observations toward 56 (Dotson et al. 2010) and 83 (Matthews et al. 2009) regions, respectively, containing mostly Galactic sources and some galaxies<sup>2</sup>. In the following we showcase an analysis of a few of these sources, based on published data, to illustrate characteristic absolute value  $|\delta|$ -patterns. An identical analysis is carried out for the additional 24 CSO sources in Appendix B.

On (large) scales, where a clear gravity center still remains to be formed, a  $|\delta|$ -map seems irregular with no clear signatures (Figure 2). In some areas, similar  $|\delta|$ -values are grouped together, other areas show a continuous change in  $|\delta|$ . Typically, specific  $|\delta|$ -values can not yet be associated with specific locations in the dust Stokes  $I$  map. This is because structures like clouds, envelopes and cores have not yet been formed. The complex CO+0.02–0.02 together with M–0.02–0.07, observed with a physical resolution  $\ell \sim 770$  mpc and covering a large area of about  $12 \text{ pc} \times 12 \text{ pc}$  (CSO, Dotson et al. (2010)), is such an example. One might speculate that such a system is still affected and shaped by its surroundings where larger scale dynamics can lead to irregular patterns (Figure 2). The correlation between magnetic field and intensity gradient position angles ( $P.A.s$ ) is not yet clearly established with more cloud-like groups (correlation coefficient  $\mathcal{C} = 0.71$ ). The histogram of  $|\delta|$  shows a rather uniform distribution with  $\langle |\delta| \rangle \approx 48^\circ$  (Middle bottom panel in Figure 2).

On a next (smaller) scale we have selected 2 sources that show elongated structures: Mon R2 ( $\ell \sim 92$  mpc) and M+0.25+0.01 ( $\ell \sim 770$  mpc over an area of about  $7.7 \text{ pc} \times 4 \text{ pc}$ ; CSO, Dotson et al. (2010)). The top and middle rows in Figure 3 reveal clear and distinct features. In the case of Mon R2 (top row), the magnetic field appears roughly perpendicular to the major axis of the Stokes  $I$  contours. Here, material is likely following the field lines (driven by gravity) leading to an elongated and possibly flattened structure with gravity also starting to pull in the field lines at the 2 ends of the major axis. As a result, the  $|\delta|$ -map shows mostly small values, except toward the 2 ends of the major axis. Here, maximum deviations of the field from the intensity gradient occur because the field is not yet clearly dragged in. The correlation,  $\mathcal{C} = 0.78$ , for such a source is tighter than for the above system CO+0.02–0.02 with M–0.02–0.07. The  $|\delta|$ -histogram shows a clear peak at small values with  $\langle |\delta| \rangle \approx 23^\circ$ . M+0.25+0.01 displays inverse features (middle row):

---

<sup>2</sup> The publicly available reduced data can be found at <http://cdsarc.u-strasbg.fr/viz-bin/qcat?J/A+A/> for the JCMT, and at <http://iopscience.iop.org/0067-0049/186/2/406/fulltext/> for the CSO.

the magnetic field is roughly along the major axis of the source. Consequently, in a  $|\delta|$ -map, the smallest values are found at the 2 ends of the major axis, with the largest deviations in between them along the axis. The correlation is systematically off ( $\mathcal{C} = 0.61$ ), which then also leads to the largest average deviation,  $\langle |\delta| \rangle \approx 57^\circ$ , of the 3 sources described here. Table 2 summarizes these results.

The collapsing core W51 e2 ( $\ell \sim 24$  mpc, Tang et al. (2009b)) yet shows different signatures on these smallest scales (bottom row in Figure 3). The source mostly appears symmetrical.  $|\delta|$ -values are generally small with  $\langle |\delta| \rangle \approx 18^\circ$ . These 2 findings might indicate that the source is already in a later phase of its collapse where gravity has pulled in and aligned the field lines with the intensity gradient. There is a trend of increasing  $|\delta|$ -values beneath and above a plane in northeast-southwest direction. Polarized emission is absent along this direction. This area likely coincides with an accretion plane (Ho & Young 1996; Zhang & Ho 1997; Young et al. 1998; Zhang et al. 1998; Solins et al. 2004; Keto & Klaassen 2008). We additionally explore this particular configuration in the next Section 2.1.2. Larger  $|\delta|$ -values as found in Mon R2 are missing here. This, however, might be due to the current limitations in resolution and/or sensitivity of the observation. There are hints of increased  $|\delta|$ -values around the emission peak. Compared to Mon R2, the zones of larger  $|\delta|$ -values appear to have shrunk and moved closer to the center. W51 e2 shows the tightest correlation between field and intensity gradient orientations with  $\mathcal{C} = 0.95$  (Table 2).

It is striking that the  $|\delta|$ -maps of the above sources Mon R2 and M+0.25+0.01 reveal clear opposite trends. Inspecting the additional 24 sources from the CSO catalog shows that these trends are also found in other sources (Appendix B). The non-uniform and incomplete polarization coverage in some sources obviously tends to erase clear features. Projection effects are unlikely mimicking these trends. It seems more plausible that certain selection effects and initial conditions from larger scales lead to one or the other case, with projection effects possibly distorting some features. Large-scale flows might initially compress the field lines, leading to structures like seen in M+0.25+0.01. Subsequently, gravity might take over and start to pull in the field lines. This will then eventually lead to a more symmetrical structure like in W51 e2. The field morphology in Mon R2 matches with an hourglass-like scenario where initially straight field lines are later pulled in by gravity leading again to an e2-type configuration. Mon R2 might be showing the beginning of such a phase.

In summary, the sources presented here seem suggestive for an evolutionary sequence where the role of the magnetic field leaves some signatures in the  $|\delta|$ -maps. In Section 4 we will add further evidence to this idea, which will allow us to conclude with a schematic scenario in Section 5.

### 2.1.2. $\delta$ in High-Resolution Cores

We highlight an additional feature of  $\delta$ -maps, focusing on high-resolution (up to  $\sim 0''.7$ ) cores observed with the SMA. Figure 4 shows  $\delta$  for W51 e2 (Tang et al. 2009b), W51 North (Tang et al. 2013), G5.89-0.39<sup>3</sup> (Tang et al. 2009a) and Orion BN/KL (Tang et al. 2010). We note that  $\delta$  is displayed in the range of  $-90^\circ$  to  $+90^\circ$ , with the sign depending on whether the magnetic field is rotated counter-clockwise or clockwise with respect to the intensity gradient. For an enhanced visual impression the data are over-gridded. The color coding makes clear that there are systematic changes in the sign of  $\delta$  between confined areas. This is particularly obvious for W51 e2 and the main cores in W51 North and Orion BN/KL. Nevertheless, even in g5.89 – where only isolated patches of polarized emission are detected, possibly due to expanding HII regions (Tang et al. 2009a) – large areas with identical signs are found. We further analyze these maps by investigating the azimuthal ( $az$ ) dependence in  $\delta$ . The top panel in Figure 5 illustrates  $\delta = \delta(az)$  for W51 e2 and the main cores in W51 North and Orion BN/KL. For all sources azimuth is measured counter-clockwise from West, with its center assumed to be at the emission peak of each source. There are seemingly ranges in azimuth where  $\delta$  is preferentially negative or positive, and there are zones where  $\delta$  changes sign. In the middle panel we have by eye re-defined the origin of the azimuth coordinate in order to align the features from the top panel. Starting from positive values around  $40^\circ$  to  $80^\circ$ , all 3 sources then show smaller and smaller values, reaching similar negative values after crossing zero. After this first zero-crossing there is a clear gap with no data for Orion BN/KL and W51 North. Then, values jump to the positive followed by a second zero-crossing over a smaller azimuth range. A clear gap is found here for W51 e2 between  $az \approx 350^\circ$  and  $az \approx 50^\circ$ . We remark that between  $az \approx 360^\circ$  and  $az \approx 0^\circ$  all sources flip sign in  $\delta$  again for a second time. Thus, aligning the features from the top panel in Figure 5 clearly reveals systematic changes in  $\delta$  with 2 fairly smooth zero-crossings and 2 zones where  $\delta$  flips sign. For comparison, the bottom panel in Figure 5 shows  $\delta$  as a function of azimuth for g5.89, where no clear features can be identified.

Figure 6 proposes an explanation for the above findings in the context of a collapsing system with accretion and outflow zones. Initially straight field lines are dragged in and bent by gravity. With respect to the intensity gradient orientations, distinct zones with negative or positive  $\delta$ -values emerge. The largest field curvature is expected in the accretion zones with  $\delta$  flipping its sign between maximum negative and maximum positive values around the accretion plane. With material mostly following the field lines and the lines being less bent toward the poles,  $|\delta|$  is decreasing toward the outflow regions. This then leads to a continuous change in  $\delta$  across zero. We remark that outflows are likely to perturb the field morphologies around the poles. Nevertheless, due to their small mass and possibly smaller dust-to-gas ratio, the currently available observations with

---

<sup>3</sup> Here and in the following sections G5.89-0.39 is abridged as g5.89.

their sensitivities and resolutions are predominantly tracing the core’s field morphology. We, thus, neglect a possible influence of the outflow in the proposed scenario here.

Remarkably, despite being illustrated for a face-on pinched field structure in Figure 6, all 3 sources in the middle panel in Figure 5 clearly reveal features matching the schematic. Nevertheless, we have to note that changes from positive to negative zones do not exactly occur within a  $180^\circ$  range in azimuth. Equally, maximum and minimum values in  $\delta$  vary with source. One might speculate that irregularities and differences are due to asymmetries and inclination/projection effects that stretch or compress certain features. In spite of these shortcomings, we can still conclude that the magnetic field azimuthal patterns in  $\delta$  provide some clues on the state of a system by identifying characteristic accretion and outflow areas. Furthermore, these features appear to be robust even in the presence of unknown inclination angles. Finally, the proposed explanation in Figure 6 naturally leads to a bimodal distribution in  $\delta$ . This has indeed been observed for W51 e2 in Figure 2 in Koch, Tang & Ho (2012a). Distributions for all high-resolution cores discussed here are displayed in Figure 7.

## 2.2. The Angle $\delta$ in the MHD Force Equation

We adopt an ideal MHD force equation as a starting point for the following derivation. As in Koch, Tang & Ho (2012a), we impose the slight restriction that the orthogonal field component is a slowly varying function, i.e.  $\frac{\Delta B_\perp}{B} \ll 1$ . This will hold for any smooth large-scale field functions<sup>4</sup>. In return, this then allows us to simplify and combine the magnetic field hydrostatic pressure and the field tension terms. With this, the force equation becomes (Koch, Tang & Ho 2012a):

$$\rho \left( \frac{\partial}{\partial t} + \mathbf{v} \cdot \nabla \right) \mathbf{v} = -\nabla P - \rho \nabla \phi + \frac{1}{4\pi} \frac{1}{R} B^2 \mathbf{n}_B, \quad (1)$$

where  $\rho$  and  $\mathbf{v}$  are the dust density and velocity, respectively.  $B$  is the magnetic field strength.  $P$  is the hydrostatic dust pressure.  $\phi$  is the gravitational potential resulting from the total mass contained inside the star forming region.  $\nabla$  denotes the gradient. The field tension force (last term on the right hand side) with the field curvature  $1/R$  is directed normal to the field line along the unity

---

<sup>4</sup> On very small scales this assumption might eventually fail for tangled magnetic fields. There is, however, no indications of such tangled fields to date from observed field morphologies. We further remark that this formalism does not rule out the existence of turbulence. In fact, the total level of turbulence  $\Delta B$  in W51 e2 was independently estimated based on a structure function (Koch, Tang & Ho 2012a). Uncertainties in observed polarization position angles due to turbulence are found to be typically 5 to  $10^\circ$ , which translates into  $\Delta B \sim \pm 1$  mG for W51 e2. This is small compared to the total field strength estimates in most positions except for the weakest ones. Thus, current observational results justify the above assumption.



vector  $\mathbf{n}_B$  (Figure 1). As usual, the inertial term on the left hand side in Equation (1) describes the resulting action based on the force terms on the right hand side.

In an observed map, the detected intensity emission is typically a function of temperature and density. We now assume that the direction of the local temperature gradient is identical or at least not too different from the local density gradient direction<sup>5</sup>. In this case, the observed intensity gradient direction on a map can be identified with the direction of the density gradient along the unity vector  $\frac{\nabla\rho}{|\nabla\rho|} \equiv \mathbf{n}_\rho$ . This connects  $\mathbf{n}_\rho$  and  $\mathbf{n}_B$  as  $\mathbf{n}_\rho \cdot \mathbf{n}_B = \cos\alpha$ , where  $\alpha$  is the angle between the intensity gradient and the originally detected polarization orientations (Figure 1, see also Figure 3 in Koch, Tang & Ho (2012a)).  $|\delta| = \pi/2 - |\alpha|$  is the angle between the magnetic field and the intensity gradient orientations analyzed in the previous sections<sup>6</sup>. We are now aiming at manipulating Equation (1) in a way that changes/variations in the morphology in a map can be attributed to the various forces. In particular, we want to link the field tension along  $\mathbf{n}_B$  to morphological features. To that purpose, we are projecting  $\mathbf{n}_B$  onto the orthonormal system  $(\mathbf{n}_\rho, \mathbf{t}_\rho)$ ,  $\mathbf{n}_B = \sin\delta \mathbf{n}_\rho + \sin\alpha \mathbf{t}_\rho$  (Figure 1), where  $\mathbf{t}_\rho$  is a unity vector tangential to the intensity contour. Equation (1) can, thus, be written as:

$$\rho \left( \frac{\partial}{\partial t} + \mathbf{v} \cdot \nabla \right) \mathbf{v} = -\nabla P - \rho \nabla \phi + \sin|\delta| \frac{1}{4\pi} \frac{1}{R} B^2 \mathbf{n}_\rho + \sin|\alpha| \frac{1}{4\pi} \frac{1}{R} B^2 \mathbf{t}_\rho. \quad (2)$$

Equation (2) provides a direct interpretation for the angle  $|\delta|$ , with some interesting insight which we are addressing in the following. Without the field tension force, the above Equation (2) would describe the dynamics governed by only the gravitational force (and a possible pressure gradient). The angle  $|\delta|$ , with  $\sin|\delta| \in [0, 1]$ , quantifies the fraction of the available field tension along the density gradient direction. Therefore,  $\sin|\delta|$  is a measure for how efficiently the magnetic field contributes to and is responsible for an observed density (emission) morphology along the gradient directions.

In the context of a collapsing system,  $\sin|\delta|$  measures how efficiently the magnetic field inhibits a collapse. In the extreme case where  $\sin|\delta| \approx 0$  ( $|\delta| \approx 0^\circ$ ), an observed density (emission)

---

<sup>5</sup> It has to be stressed that the temperature does *not* have to be constant. Neither requires the above argument that the temperature changes more slowly than the density. The temperature can even change faster as long as its direction aligns roughly with the density gradient direction. *Locally* identifying  $\nabla\rho$  with the intensity emission gradient only needs the *local directions* of temperature and density gradients to be aligned. Thus, regions of different temperatures do not pose a problem in our approach, as long as temperature changes are accompanied by density changes toward roughly the same direction.

<sup>6</sup> The angle  $\delta$  is always defined as the smaller of the 2 complementary angles to  $\pi$  at the interception of field and intensity gradient orientations; i.e.  $\delta$  is always in the range between 0 and  $+\pi/2$ . Absolute values are used in the equations here because  $\delta$  can also be given a sense of orientation (Section 2.1.2).

gradient is aligned with the field. Consequently, for any field strength, the magnetic field does not influence the local structure along the density gradient direction. In a close-to-circular e2-type system, the local dynamics along the gradient directions, i.e. in radial direction, proceed as if the field does not exist (Equation (2)). The dynamics in radial direction  $\mathbf{n}_\rho$  are entirely and only driven by the gravitational force  $\rho \nabla \phi$  (with a likely negligible pressure gradient  $\nabla P$ ). In other words, in this situation the field plays a very minor role compared to gravity. This conclusion is consistent with our result in Koch, Tang & Ho (2012b) where the field-to-gravity force ratio  $\Sigma_B$  is calculated to be  $\sim 20\%$  in the e2 core. Nevertheless, Equation (2) shows that a tangential force component depending on field strength and curvature is also present. For pulled-in relatively straight field lines, a small curvature (large  $R$ ) will suppress this component. Closer to the center, an increasingly smaller curvature radius might lead to additional dynamics in tangential direction. In the other extreme case when  $\sin|\delta| \approx 1$  ( $|\delta| \approx 90^\circ$ ), the magnetic field maximally contributes to an observed morphology along the density gradient direction. Besides the orientation of the field with the density gradient, the absolute field strength is also relevant here. With  $\sin|\delta| > 0$ , the field will always work against gravity, slowing down gravity<sup>7</sup> at a maximum when  $|\delta| = 90^\circ$ . At such locations we would generally expect a density gradient that is less steep with emission contours that are spaced further apart. The tangential force component in Equation (2) is negligible here.

In summary, different values in the angle  $|\delta|$  reflect regions with different dynamics. The larger  $|\delta|$ , the more important the field is dynamically in working against gravity. This is also consistent with a decreasing force ratio  $\Sigma_B$  with smaller radius in a collapsing core as derived in Koch, Tang & Ho (2012b).

### 3. Magnetic Field Quantities

Here, we provide a brief summary and comparison of the magnetic field parameters resulting from our work so far (Section 3.1). Besides the angle  $\delta$  introduced in the previous section, we have already derived a technique to estimate the local magnetic field significance  $\Sigma_B$  and the local field strength  $B$  in Koch, Tang & Ho (2012a). In Section 3.2 we demonstrate how these 2 different studies are connected. A detailed discussion on the relevant assumptions is given in Appendix A.

---

<sup>7</sup> This is certainly the case where gravity is bending the field lines and dragging them in, as e.g., in a collapsing system as discussed here. We, however, have to acknowledge that, generally speaking,  $\mathbf{n}_B$  in Figure 1 could also point in opposite direction if the field line is bent the other way. In such a case, the projection onto the same orthonormal system ( $\mathbf{n}_\rho, \mathbf{t}_\rho$ ) will lead to opposite signs in the Equation (2). This ambiguity can be overcome by introducing a sign for the field curvature,  $\pm 1/R$ , for a convex or concave field shape.

### 3.1. $\Delta_B$ , $\Sigma_B$ and $B$ – A Summary

The combination of the three parameters –  $\sin|\delta|$ ,  $\Sigma_B$  and  $B$  – characterizes and quantifies the local role of the magnetic field:

$$\text{field alignment deviation: } \Delta_B = \sin|\delta|, \quad (3)$$

$$\text{relative field significance: } \Sigma_B = \frac{\sin\psi}{\sin\alpha} = \frac{\Delta_G}{\sqrt{1-\Delta_B^2}}, \quad (4)$$

$$\begin{aligned} \text{absolute field strength: } B &= \sqrt{\frac{\sin\psi}{\sin\alpha} (\rho\nabla\phi + \nabla P) \cdot 4\pi R} \\ &= \sqrt{\Sigma_B (\rho\nabla\phi + \nabla P) \cdot 4\pi R}, \end{aligned} \quad (5)$$

where we have introduced the new symbols  $\Delta_B \equiv \sin|\delta| = \cos\alpha$  for the field deviation and  $\Delta_G \equiv \sin\psi$  for the gravity alignment deviation,  $\psi$  being the angle between the intensity gradient and the gravity and/or pressure force orientation (Figure 1 and Figure 3 in Koch, Tang & Ho (2012a)). The field strength  $B$  and its relative significance  $\Sigma_B$  compared to the gravity and/or pressure forces are analyzed in detail in Koch, Tang & Ho (2012a,b).

We stress that both  $\Sigma_B$  and  $\Delta_B$  rely only on measurable angles. Thus, both parameters are independent of any mass and field strength assumptions and any further modeling of a molecular cloud. The two quantities are solely based on angles which reflect the field and dust morphologies that are the overall result of all the forces acting in the system. The relative field significance  $\Sigma_B$  leads to the total field strength  $B$  when adding the mass and density information. This breaks the degeneracy in the dimensionless ‘scale-free’ quantities based on angles only, and connects them to each individual physical system. The order of magnitude of the field strength is, thus, largely determined by the mass, with  $\Sigma_B$  quantifying the fraction of this mass that can be balanced by the field. Whereas  $\Sigma_B$  compares locally the field force to the other forces,  $\Delta_B$  measures how much of the maximally available field tension force is taking part in the dynamics along the gradient direction. Thus,  $\Delta_B$  is constrained to an upper limit of 1, whereas  $\Sigma_B$  has no upper limit and can be larger than one if the field is dominating. Table 1 compares the properties of these three field parameters.

### 3.2. Linking $\Delta_B$ and $\Sigma_B$

Figure 8 illustrates the connection between field and gravity deviations,  $\Delta_B$  and  $\Delta_G$ , and the field significance  $\Sigma_B$  based on Equation (4). Small values in the deviation  $\Delta_B$  – i.e., close alignment between magnetic field and intensity gradient orientations – minimize the contribution of the field tension term along the density gradient direction in Equation (2). This is already

suggestive for a rather minor role of the magnetic field in this situation. Nevertheless, this criterion alone does not yet provide any information on the field compared to the other forces in Equation (2). This caveat is overcome with the field significance  $\Sigma_B$  (as a result from the polarization - intensity gradient method). And indeed, this reveals that the field significance scales roughly as  $\sim \Delta_G \equiv \sin \psi \lesssim 1$  for small values in  $\Delta_B$ . Thus, for most of the parameter space, the field is indeed of minor importance compared to other forces (Figure 8). Only for large values in  $\Delta_G \sim 1$ ,  $\Sigma_B$  can equal unity or become slightly larger. Intuitively this is expected, because growing values in  $\Delta_G$  indicate larger deviations in the intensity gradient direction from the gravity center which have to be caused by a growing presence of the magnetic field.

As  $\Delta_B$  grows, the field becomes more relevant for the dynamics along the density gradient direction in Equation (2). Therefore, we expect the field to take on a more important role in shaping and influencing an observed dust continuum morphology. Additionally bringing in  $\Sigma_B$ , we can indeed confirm that the relative field significance  $\Sigma_B$  is growing as  $1/\sqrt{1-\Delta_B^2}$  for constant values in  $\Delta_G$  (dotted magenta lines in Figure 8). The larger  $\Delta_G$  already is, the faster  $\Sigma_B$  passes unity. Or, in other words, for any existing deviation in the intensity gradient from the gravity direction, an additionally growing deviation with the field orientation reflects a growing field importance. This growth in field significance, nevertheless, does not yet automatically mean that the field is dominating. The gray dotted line in Figure 8 separates the  $(\Delta_G, \Delta_B)$ - parameter space into  $\Sigma_B < 1$  and  $\Sigma_B > 1$ .<sup>8</sup>

In summary, whereas  $\sin|\delta| \equiv \Delta_B$  in Equation (2) is already indicative for the role of the magnetic field,  $\Sigma_B$  further sharpens and quantifies this by additionally taking into account the information of the other forces in the system (i.e.,  $\Delta_G$ ). It has to be stressed that introducing  $\sin|\delta|$  in Equation (2) and deriving  $\Sigma_B$  with the polarization - intensity gradient method are two independent approaches. As a sole common ground, they start with an ideal MHD force equation, but then proceed with two different assumptions. A comparison and validity of these two assumptions is given in Appendix A.

#### 4. $|\delta|$ - Map: A Tracer for the Change in the Role of the Magnetic Field

As explained in Section 2, the angle  $\delta$  can be directly linked to the (projected) MHD force Equation (2). Nevertheless, the role and the significance of the magnetic field – the field tension in the rightmost term in Equation (1) – are not yet explicitly visible due to the (unknown) gravitational force term. Additionally, the angle  $\delta$  can be affected by projection effects. The magnetic

---

<sup>8</sup>Note that the boundary zone with  $\Delta_B \equiv 1$  (except  $\Delta_B = 1$  with  $\Delta_G = 0$ ) is, strictly speaking, excluded because the method is failing here.

field-to-gravitational force ratio  $\Sigma_B$  (Section 3 and Koch, Tang & Ho (2012a)) can overcome these shortcomings and links the magnetic field tension to the gravity in a system via the polarization - intensity gradient method. Moreover, projection effects are minimized in  $\Sigma_B$  or even cancel out.

In the following sections, we further investigate the connection between  $\delta$  and  $\Sigma_B$ , with the goal of establishing  $\delta$  as a tracer for the change in the role of the magnetic field over an observed map. This is motivated by the aim of providing a simple tool ( $|\delta|$ -map, Section 2.1) to interpret polarization data. Whereas calculating  $\Sigma_B$  requires a more elaborate modeling, the angle  $\delta$  can be readily read off from a map once intensity gradient orientations are derived. Often, a simple inspection by eye will already allow for differentiating between clearly small or large  $\delta$ -values. This, in contrast, is non-trivial for  $\Sigma_B$ . There is, thus, a substantial benefit from gaining further insight in  $\delta$  and its deeper connection to  $\Sigma_B$ .

#### 4.1. Approximating $\Sigma_B$

We start by addressing the concern of projection effects in  $\delta$ . For any observable, projection effects cancel out when looking at the relative change (logarithmic derivative) of this observable. Assuming the 3-dimensional (lower index '3') deprojected angle  $\delta_3$  linked with an inclination angle  $\iota_B$  to the projected 2-dimensional (lower index '2') angle  $\delta_2$ ,  $\Delta_{B_3} = \sin \delta_3 = \sin \delta_2 \cdot \cos \iota_B$  (see Figure 13 in Koch, Tang & Ho (2012a)), we can write the logarithmic derivative:

$$\frac{d(\Delta_{B_3})}{\Delta_{B_3}} = \frac{d(\sin \delta_2 \cdot \cos \iota_B)}{\sin \delta_2 \cdot \cos \iota_B} = \frac{d(\sin \delta_2)}{\sin \delta_2} = \frac{d(\Delta_{B_2})}{\Delta_{B_2}}. \quad (6)$$

$d$  denotes the total differential, and we have assumed  $d(\cos \iota_B) \equiv 0$ . In the previous Section 2, lower indices '2' were omitted for map-projected quantities. In practice, we are interested in changes in  $\delta$  from one pixel to its neighboring pixels in a map, in order to assess the change in the role of the magnetic field. It is, thus, a very mild assumption to impose no change in the inclination angle, i.e.  $d(\cos \iota_B) = 0$ , between adjacent pixels. If necessary, this condition can be relaxed to  $d(\cos \iota_B) \approx 0$  or very small, which will still leave the above equation correct on a pixel-to-pixel basis, but would allow for a change in inclination from one end to another end in a map, if this should seem plausible. The logarithmic differential for the field significance  $\Sigma_B$ , Equation (4), can then be written as:

$$\frac{d\Sigma_B}{\Sigma_B} = \frac{1}{\Delta_G} \cdot d(\Delta_G) + \frac{\Delta_B}{1 - \Delta_B^2} \cdot d(\Delta_B), \quad (7)$$

where we have again omitted the lower indices '2' for the map-projected quantities  $\Delta_G$  and  $\Delta_B$ . In Equation (7) the magnetic field alignment deviation  $\Delta_B$  and the gravity alignment deviation  $\Delta_G$  are decoupled into additive terms quantifying their relative contributions to  $d\Sigma_B/\Sigma_B$ . We re-define

their individual contributions as:

$$\Xi_B = w_B \cdot d(\Delta_B) \quad \text{and} \quad \Xi_G = w_G \cdot d(\Delta_G), \quad (8)$$

where we have introduced the weight functions  $w_B = \frac{\Delta_B}{1-\Delta_B^2}$  and  $w_G = \frac{1}{\Delta_G}$  for the magnetic field and gravity, respectively. A change in the field significance,  $d\Sigma_B/\Sigma_B$ , generally depends on the 4 parameters  $\Delta_B$ ,  $\Delta_G$ ,  $d(\Delta_B)$  and  $d(\Delta_G)$ . For simplicity, we assume here first  $d(\Delta_B) \approx d(\Delta_G) \approx \text{const}$ , i.e. we assume roughly similar (small) changes in the field and gravity alignment deviations from one pixel to the next one. This then allows us to simplify Equation (7) to 2 variables and compare the weight functions  $w_B$  and  $w_G$  in their relevance for  $\Sigma_B$  (Figure 9). This leads to some remarkable insight: (1) For any values in  $\Delta_G$ , small values in  $\Delta_B$  (small values in  $\delta$ ) always mean that the magnetic field is irrelevant for a change in  $\Sigma_B$ . A change in  $\Sigma_B$  is dominated by gravity and for  $d(\Delta_B) \approx d(\Delta_G)$  the field is not important and thus,  $\Sigma_B < 1$ . (2) For any value in  $\Delta_G$ , and  $\Delta_B \leq 0.618$  ( $|\delta| \lesssim 38^\circ$ ), the magnetic field is less important or at most equally important to a change in  $\Sigma_B$ . (3) For values  $\Delta_B > 0.618$  ( $|\delta| \gtrsim 38^\circ$ ), the magnetic field can (but does not necessarily) dominate gravity. If  $d(\Delta_G)$  and  $d(\Delta_B)$  are known, the weight functions in Figure 9 can accordingly be shifted vertically.

The above conclusions compare magnetic field and gravity force. We can additionally formulate 2 consequences from Figure 9 for the magnetic field separately: (1) Small values in  $\Delta_B$  (small values in  $|\delta|$ ) *always minimize* the field contribution to  $d\Sigma_B/\Sigma_B$ . (2) Large values in  $\Delta_B$  (large values in  $|\delta|$ ) *always maximize* its contribution. This is true for any values in  $\Delta_G$  and  $d(\Delta_G)$ .

We have to acknowledge that most of the above conclusions can also be found from  $\Sigma_B$  (Equation (4)). What have we gained from further analyzing the above logarithmic differential? We recall that we are aiming at establishing  $|\delta|$ -maps as a tracer for the change in the role of the magnetic field. Interestingly, the weight function  $w_B = \frac{\Delta_B}{1-\Delta_B^2}$  is close to  $|\delta|$  ( $\Delta_B = \sin|\delta|$ ), only with an additional factor  $\frac{1}{1-\Delta_B^2}$ . Since  $1 - \Delta_B^2 \leq 1$ ,  $\sin|\delta|$  thus always provides a lower limit to a change in the field significance (blue dashed line in Figure 9). For values  $\Delta_B \lesssim 0.5$  ( $|\delta| \lesssim 30^\circ$ ),  $\sin|\delta|$  is even accurate to within about 25% of  $w_B$ . The logarithmic differential in Equation (7) has, therefore, allowed us to explicitly put  $|\delta|$  in relation with the projection-free quantity  $d\Sigma_B/\Sigma_B$ , thus establishing  $|\delta|$  as a valid approximation for it.

In summary, whatever the value for  $\Xi_G$ ,  $\Xi_B$  can always be approximated with  $|\delta|$ . Therefore,  $|\delta|$ -maps by themselves – despite possibly being affected by projection effects – already reflect the change in the role of the magnetic field in a system. An increase (decrease) in  $|\delta|$  will indicate an increase (decrease) in  $\Sigma_B$ , and thus, point toward a growing (diminishing) significance of the field as compared to gravity.

## 4.2. Comparing $|\delta|$ -Map and $\Sigma_B$ -Map

It remains to test in practice how reliably a  $|\delta|$ -map – in the presence of (unknown) projection effects – reflects the role of the magnetic field. To that purpose,  $\Sigma_B$ -maps – mostly free of projection effects – are shown for comparison in Figure 10. All 3 sources, Mon R2, M+0.25+0.01 and W51 e2 show structures in their  $\Sigma_B$ -maps that seem to have analogous features in their  $|\delta|$ -maps (Figure 3, right panels). Regions with small  $|\delta|$ -values,  $\sim 0\text{--}20^\circ$ , in Mon R2 mostly coincide with  $\Sigma_B$ -values below 0.5. Maximum field-to-gravity ratios around 1 are found at the 2 ends of the source major axis in a northeast-southwest direction, which is also where the  $|\delta|$ -values peak around  $60^\circ$ . The right panel in Figure 10 shows this positive correlation between  $\Sigma_B$  and  $|\delta|$  with a growing spread in  $\Sigma_B$  for increasing  $|\delta|$ -values. The smaller-scale e2 core (Figure 10, bottom panels) reveals a similar result. The immediate core area with  $|\delta| \lesssim 30^\circ$  (Figure 3) shows force ratios  $\Sigma_B \lesssim 0.5$ . In the newly forming core in the northwest extension  $\Sigma_B$  increases to about 1.5. Its maximum values are found to coincide with the maximum  $|\delta|$ -values around  $50^\circ$ . Additionally, there is a hint of larger  $\Sigma_B$ -values toward the accretion plane in the upper northern half of the core. The same tendency is again found in the  $|\delta|$ -map. As for the case of Mon R2, the  $\Sigma_B - |\delta|$ -plot again reveals a positive correlation with a smaller dispersion for small  $|\delta|$ .

The source M+0.25+0.01 – with its magnetic field mostly aligned with the source major axis – reveals inverse patterns in its  $|\delta|$ -map (Figure 3, middle row), as compared to Mon R2 and W51 e2. Regions with small values in  $|\delta|$  are found only in the north and south. In most areas, the magnetic field - intensity gradient deviations  $|\delta|$  are large, up to  $80\text{--}90^\circ$ . Strikingly, the  $\Sigma_B$ -map in Figure 10, middle panel, shows a tight correlation both for the zones of small and large values. Zones with  $\Sigma_B \lesssim 0.5$  are found only in the north and south and at a few locations between a Dec offset  $\approx 0$  and  $\approx 50$ . In between these areas, the magnetic field significance is growing to values where the field tension force is dominating gravity by a factor of up to 10 or more. The  $\Sigma_B - |\delta|$ -plot shows a linear relation up to  $|\delta| \approx 60^\circ$ , with an exponentially growing field significance  $\Sigma_B$  for the largest deviations around  $80\text{--}90^\circ$ . This is expected because large values in  $|\delta|$  will boost  $1/\sin \alpha$  in  $\Sigma_B$ .

Contrary to Mon R2 and W51 e2 where maximum values in  $\Sigma_B$  are around 1 and 1.5, M+0.25+0.01 reveals a much more dominating field in most areas. Nevertheless, all 3 sources manifestly show a positive correlation between  $|\delta|$  and  $\Sigma_B$ . We, therefore, conclude that  $|\delta|$  indeed can trace the change in the magnetic field significance. We stress that we conservatively focus on the *change* in the magnetic field role / significance because from a range of  $|\delta|$ -values we can not yet conclude a range of  $\Sigma_B$ -values; e.g., the  $\sim 40\text{--}60^\circ$  range in Mon R2 covers  $\Sigma_B$  up to  $\sim 1$ , whereas the same range in M+0.25+0.01 is more likely to point toward  $\Sigma_B \sim 2$ . This is a consequence of the missing information from the angle  $\psi$  (and some possibly related projection effect) when looking at  $|\delta|$  only. This explains and defines the dispersion in  $\Sigma_B$  for a fixed  $|\delta|$ -value. Due to this scatter,

disconnected patches in  $|\delta|$ -values will be of limited information. Changes of  $|\delta|$  over an entire source, nevertheless, show an overall positive correlation with  $\Sigma_B$  and, therefore, reliably describe the varying role of the magnetic field with position.

An identical analysis of a larger sample of 24 CSO sources (Dotson et al. 2010) is presented in Appendix B. In the large majority of these sources, features in  $\Sigma_B$ -maps are also reflected in  $|\delta|$ -maps. Occasional incomplete polarization coverages can limit this resemblance. From the total sample of 31 sources – 27 from the CSO and 4 from the SMA – we arrive at a main conclusion: changes in the field significance  $\Sigma_B$  are revealed by changes in the angle  $|\delta|$ . On average, larger angles  $|\delta|$  are pointing toward larger  $\Sigma_B$ -values, thus indicating a dynamically more significant magnetic field. Basic statistical quantities are summarized in Table 2.

## 5. Schematic Scenario

The previous sections have established the angle  $|\delta|$  as a reliable tracer for the change in the role of the magnetic field. This is a consequence of 2 main results: (1) the angle  $|\delta|$  can be interpreted as a field alignment deviation (efficiency) in the MHD force equation; (2) the angle  $|\delta|$  always yields an approximation (lower limit to the magnetic field weight function  $w_B$ ) to a change in the field significance  $\Sigma_B$ . Figure 10 and Appendix B demonstrate and confirm the expected connection between  $|\delta|$  and  $\Sigma_B$ . In the following, we now propose an evolutionary scenario, across which the role of the magnetic field can be assessed with the angle  $|\delta|$ .

Similarities and analogous features are apparent between  $|\delta|$ -maps (Figure 2 and 3) and  $\Sigma_B$ -maps (Figure 10). In Figure 11 we adopt CO+0.02–0.02-, M–0.02–0.07-, M+0.25+0.01-, Mon R2- and W51 e2-type sources as prototype sources with clear  $|\delta|$ - (and consequently  $\Sigma_B$ -) structures. The competition between the magnetic field tension and other forces is reflected in distinct  $|\delta|$ -patches. In an early phase – labeled as (I) in Figure 11 – larger scale dynamics in the surroundings lead to initial mass shuffling, leading to density contrasts but not yet well-defined shapes with clear gravity centers. Patches with different  $|\delta|$ -values appear. The absence of clear gravity centers leads to more random-like  $|\delta|$ -structures that are less organized without clear symmetry features. Nevertheless, areas with small (large)  $|\delta|$  point toward a minor (dominant) role of the magnetic field compared to other forces like gravity and/or pressure gradients. On these largest scales in (I), some regions might already reveal themselves as to what type of magnetic field - density configuration they will develop into. The dotted squares in (I) illustrate areas that are likely to evolve into (IIA) and (IIB) in a later phase. Elongated structures of two types can be formed, with either a mean magnetic field orientation roughly perpendicular (IIA) or roughly parallel (IIB) to the density major axis. One can speculate that certain initial configurations in (I) will either preferentially lead to (IIA) or (IIB): gravity possibly has just started to shape the (IIA)-precursor region, whereas



large-scale flows and/or turbulence seem more plausible to create the elongated structure in the (IIB)-precursor region with the field being compressed perpendicular to its mean orientation. For any of these two regions, gravity is growing more important in (IIA) and (IIB) as the field lines are being pulled in. Due to the different initial configurations,  $|\delta|$ -maps will reveal opposite trends here. The largest deviations in (IIA) are found at the two ends of the dust emission major axis where the field maximally resists gravity. The field significance  $\Sigma_B$  is maximum here. On the other hand, the same areas in (IIB) show field orientations that are closely aligned with the dust emission gradients, minimizing  $|\delta|$  and  $\Sigma_B$ . Outside of these areas,  $\Sigma_B$  is growing and diminishing in (IIB) and (IIA), respectively. As gravity leads to further contraction, these elongated structures are more symmetrized in (III). Areas with large and small  $|\delta|$  move closer together. Zones with maximum  $|\delta|$ - and  $\Sigma_B$ -values are likely shrunk and moved closer to the center (yellow dashed patches in (III)), leaving more field lines closer to radial directions (green dashed patches in (III)). In this way, the initially different configurations (IIA) and (IIB) might evolve into one and the same system (III). This (smaller-scale) system can then be further analyzed using the symmetry properties of  $\delta$  (including its sign) as introduced in Section 2.1.2. Thus, in this sequence of evolution, symmetries, features and changes in  $|\delta|$  (and  $\delta$ ) reveal the role of the magnetic field. A minor or dominant role of the field can be classified via  $|\delta|$ . A more quantitative estimate is achieved via  $\Sigma_B$ .

Many of the additional sources presented in Appendix B can be categorized as (IIA) or (IIB). Essentially no source is found that qualifies as (III) because the CSO  $20''$  resolution typically does not fully reveal the densest core structures. We note that a thorough analysis of mean polarization orientations versus source shapes is presented in Tassis et al. (2009). Whereas in their work differences in mean orientations are compared with the source aspect ratios, we are making use of the  $|\delta|$ -distributions. By looking at broad features in these distributions – i.e., peaking toward small values versus peaking toward large values – a simple bimodal categorization is possible. Offsets of roughly perpendicular or roughly parallel can still be identified with a peak and can, therefore, still be categorized as (IIA) and (IIB). Table 2 summarizes our results. Sources are tentatively categorized as (I), (IIA), (IIB) or (III) by visual inspection of  $|\delta|$ -maps and distributions. A more thorough statistical analysis of Table 2 will be presented in a forthcoming work.

## 6. Summary and Conclusion

Based on the observed angle  $\delta$  between magnetic field and dust emission gradient orientations, we propose a generally valid interpretation for the role of the magnetic field. This then further leads to a schematic scenario for the magnetic field in the evolutionary phases from large-scale systems to collapsing cores. The key points are summarized in the following.

1. *Observed angle  $|\delta|$ :* Magnetic field and dust emission gradient orientations are observed to show distinct patterns and symmetry features. This is both found in lower- resolution CSO and higher-resolution (sub-)arcsecond SMA data. The angle  $|\delta|$  between these two orientations is straightforward to observe, does not rely on any modeling and can often already be estimated by eye.  $|\delta|$ -histograms and correlation coefficients reflect ensemble-averaged properties and differences.
2. *Observed high-resolution cores:* SMA high-resolution (collapsing) cores reveal additional symmetry properties in  $\delta$  when taking into account the relative orientation between magnetic field and dust emission gradient. These features can be explained assuming a core with accretion and outflow zones. These findings seem to be preserved even in the presence of possibly unknown projection effects.
3.  *$|\delta|$  in the MHD force equation:* When identifying an observed intensity gradient orientation with the density gradient orientation in the MHD force equation, the magnetic field tension force term can be written with an additional factor  $\sin|\delta|$ . The angle  $|\delta|$  then measures to what extent the field tension force contributes to an observed density gradient. Thus,  $\sin|\delta|$  can be interpreted as a field alignment deviation or a field deviation efficiency.
4.  *$|\delta|$ -map tracer:* Taking into account projection effects, it can be demonstrated that a  $|\delta|$ -map always yields an approximation (lower limit to the magnetic field weight function  $w_B$ ) to the more elaborate  $\Sigma_B$ -map which fully quantifies the magnetic field significance. Moreover, we show in practice, that positional changes in a  $|\delta|$ -map closely reflect changes in a  $\Sigma_B$ -map. Therefore, we generally propose  $|\delta|$ -maps as reliable tracers for the change in the role of the magnetic field over an observed map.
5. *Schematic evolutionary scenario:* Symmetries and features in  $|\delta|$ -maps (and consequently in  $\Sigma_B$ -maps) evolve from larger-scale cloud complexes to collapsing cores. On the largest scales, apparently random  $|\delta|$ -patches are found which point toward a variable magnetic field influence. In a next phase, elongated structures appear with a mean field orientation either roughly parallel or orthogonal to the major axis of the structure. The field is here more dominant toward either the center or toward the two ends of the major axis. In a later third phase, gravity leads to less elongated but more symmetrized (collapsing) cores. Here,  $\delta$  can reveal zones of accretion and outflows. In many areas, the field is increasingly radially aligned, illustrating its diminishing role in this phase.

The authors acknowledge the referees for very careful and thorough comments that led to further insight in this work. P.T.P.H. is supported by NSC Grant NSC99-2119-M-001-002- MY4.

## Appendix

### Appendix A – About the Intensity Gradient

The derivation of the angle  $\delta$  in Equation (2) with its interpretation as field alignment deviation (Equation (3)) is based on identifying an observed intensity gradient direction with the density gradient direction. This might seem at odds with the assumption in Koch, Tang & Ho (2012a), where the intensity gradient is identified with the orientation of the inertial term on the left-hand side in the MHD force equation (1). The assumption in Koch, Tang & Ho (2012a) is phenomenologically motivated, by picturing a gradient in emission as a consequence of accumulating and compressing material. Such a process is the result of all the combined forces acting in a molecular cloud and is, therefore, measured with the inertial term. The assumption then states that the emission gradient must have some of this information of the inertial term encrypted in its direction. We stress that – in both the derivation of the force ratio  $\Sigma_B$  and the local field strength – only the direction of the emission gradient but not its magnitude is relevant.

In the following we compare these two assumptions – (a) emission gradient direction measures density gradient direction and (b) emission gradient direction is a measure for inertial term direction – by further analyzing the inertial term in Equation (1). We assume stationarity, i.e.  $\partial/\partial t \equiv 0$ <sup>9</sup>. Using a vector identity, the inertial term can then be written as  $\rho(\mathbf{v} \cdot \nabla)\mathbf{v} = -\rho\mathbf{v} \times (\nabla \times \mathbf{v}) + \rho\nabla(1/2\mathbf{v}^2)$ . Since we are interested in its connection to the density gradient  $\nabla\rho$ , we are making use of  $\nabla(\rho v^2) = \rho\nabla v^2 + v^2\nabla\rho$ . This then leads to:

$$\rho(\mathbf{v} \cdot \nabla)\mathbf{v} = -\rho\mathbf{v} \times (\nabla \times \mathbf{v}) + \frac{1}{2}\nabla(\rho v^2) - \frac{1}{2}v^2\nabla\rho, \quad (9)$$

where  $v$  is the absolute value of the velocity  $\mathbf{v}$ . The first term on the right-hand side depends on the curl of the velocity field. For a curl-free flow or for a curl small compared to a density change over the resolution of an observation, this term can be neglected. Otherwise, the curl of a velocity field being along the rotation axis that is normal to the plane where the velocities change, the direction of the term  $\mathbf{v} \times (\nabla \times \mathbf{v})$  is in the plane of the velocity flow. The second term describes a change in ram pressure. The change along a density gradient direction is measured with the third term.

Based on Equation (9) we can now distinguish two main situations first: (i) *The velocity field has a negligible curl and the velocity is aligned with the density gradient*: A density change occurs along a velocity direction. The direction of the inertial term follows the den-

---

<sup>9</sup>If necessary, this condition of strict stationarity can be relaxed by considering time scales  $\Delta t$  where changes in velocity are small compared to typical changes per resolution element  $\Delta R$ , i.e.  $\Delta\mathbf{v}/\Delta t \ll \Delta\mathbf{v}/\Delta R$ . In such situations,  $\Delta\mathbf{v}/\Delta t$  will then not significantly alter the direction of the inertial term.

sity gradient<sup>10</sup>. (ii) *The velocity field has a negligible curl, but the velocity direction is different from the density gradient direction:* In order to analyze this general case, we approximate the differential operators on the right-hand side in Equation (9) as changes per resolution element  $\Delta R$ :  $1/2 \nabla (\rho v^2) - 1/2 v^2 \nabla \rho \sim -1/2 v^2 \Delta \rho / \Delta R \mathbf{n}_\rho + 1/2 (v^2 \Delta \rho / \Delta R + 2 \rho v \Delta v / \Delta R) \mathbf{e}_v$ , where  $\mathbf{e}_v$  is a unity vector tangential to a streamline<sup>11</sup>. We additionally make use of the continuity equation with  $\partial \rho / \partial t \approx 0$ , thus giving  $\mathbf{v} \cdot \nabla \rho + \rho (\nabla \cdot \mathbf{v}) = 0$ . Introducing the angle  $\eta$  between the velocity and the density gradient directions (Figure 12) together with again approximating the differential operators in the continuity equation with the resolution elements  $\Delta R$ , leads to  $(\Delta v / \Delta R) / v \sim -\cos \eta (\Delta \rho / \Delta R) / \rho$ . This relation states that any relative change in velocity (relative to the absolute velocity) is balanced by a relative change in density modulo the alignment factor  $\cos \eta$ . This then allows us to express the above approximation in terms of  $\Delta \rho / \Delta R$  only:

$$-\frac{1}{2} v^2 \frac{\Delta \rho}{\Delta R} \mathbf{n}_\rho + \frac{1}{2} \left( v^2 \frac{\Delta \rho}{\Delta R} + 2 \rho v \frac{\Delta v}{\Delta R} \right) \mathbf{e}_v = -\frac{1}{2} v^2 \frac{\Delta \rho}{\Delta R} [\mathbf{n}_\rho + (2 \cos \eta - 1) \mathbf{e}_v]. \quad (10)$$

Equation (10) is an estimate of the inertial term, neglecting the curl and approximating differential operators with changes per resolution element  $\Delta R$ . In particular, the direction of the inertial term – which is relevant for the polarization- intensity gradient method – is now linked to the density gradient and the velocity direction with the expression in square brackets. We now investigate this term further, with the goal of quantifying the resulting deviation  $\epsilon$  from the direction of the density gradient  $\mathbf{n}_\rho$  (Figure 12). The alignment angle  $\eta$  between  $\mathbf{n}_\rho$  and  $\mathbf{e}_v$  is in the range of 0 to 90°. Therefore, the factor  $(2 \cos \eta - 1)$  changes sign at  $\eta = 60^\circ$ , defining two different regimes where  $\mathbf{e}_v$  is either added to or subtracted from  $\mathbf{n}_\rho$ . Figure 13 displays the inertial term deviation  $\epsilon$  from the density gradient as a function of  $\eta$ . For  $\eta$  within 60°, the maximum deviation is about 14° with an average of 8.8°. These relatively small deviations are a consequence of the continuity equation which controls the magnitude  $(2 \cos \eta - 1)$  along the velocity direction  $\mathbf{e}_v$ . For angles  $\eta > 60^\circ$ , the deviation  $\epsilon$  grows linearly to a maximum of  $-45^\circ$  where  $\mathbf{e}_v$  is orthogonal to  $\mathbf{n}_\rho$  (red regime in Figure 13). The overall average deviation, including extreme values  $\eta > 60^\circ$ , is  $\langle \epsilon \rangle \approx 17^\circ$ .

The analysis here makes clear that the possible difference between velocity and density gradient directions plays a major role in how closely the two assumptions (a) and (b) agree. The

---

<sup>10</sup> A hydrodynamical collapse, or a close-to-hydrodynamical collapse is an example for this situation. In a spherically symmetrical collapse model, density gradients and accelerations only occur in radial direction. Independent of any symmetries, if compression (roughly uniform over a resolution element) happens along streamlines, inertial term and density gradients will be aligned.

<sup>11</sup> In writing so, we assume that a dominating change in ram pressure (over a resolution element) is directed along a (bulk) streamline, i.e., we are omitting a possible component  $\nabla (\rho v^2)_\perp$  orthogonal to a bulk flow. Note that this does not strictly exclude the existence of turbulence. Turbulence can exist up to a level such that a dominating organized bulk flow (in a resolution element) can still be identified.

presence of a significant velocity curl in Equation (9) might lead to an additional more complicated dependence of  $\epsilon$  on  $\eta$ . We are not attempting to quantify this here. Further investigations via numerical simulations will be more appropriate to tackle down the detailed influence of a curl term. We are, thus, left with average deviations of about  $8.8^\circ$  to about  $17^\circ$  between a measured emission gradient direction and the inertial term direction. These are conservative estimates while assuming no significant velocity curl over a beam-averaged resolution element. We now recall that uncertainties in polarization position angles from observations are typically in the range of about  $5$  to  $10^\circ$ . Errors in the emission gradient orientations are slightly smaller,  $\sim 3$  to  $5^\circ$ , due to averaging in the interpolation when calculating the gradient. Additional statistical uncertainties in the field orientation resulting from turbulent dispersion are also around  $5$  to  $10^\circ$  (Koch, Tang & Ho 2010). We, therefore, conclude that adopting the emission gradient orientation is a reasonably good approximation for the orientation of the inertial term in the polarization–intensity gradient method. Furthermore, in the presence of other (statistical) uncertainties, the overall error budget is not significantly affected.

Finally, we propagate the uncertainty in the orientation of the inertial term, i.e., the deviation  $\epsilon$ , through to the magnetic field significance  $\Sigma_B$  and the field strength  $B$ . To that purpose, we replace  $\sin\psi/\sin\alpha$  with  $\sin(\psi+\epsilon)/\sin(\alpha-\epsilon)$  in the Equations (4) and (5). Figure 14 displays the expected errors in  $\Sigma_B$  and  $B$  for  $\langle\epsilon\rangle \approx 8.8^\circ$  as a function of the angles  $\alpha$  and  $\psi$ . For most of the  $(\alpha, \psi)$ –parameter space, errors are less than 50%. Larger errors are typically limited to small angles  $\alpha$ . This is, however, less of a consequence of the deviation  $\epsilon$  than the result of the factor  $1/\sin\alpha$  that amplifies any error for small values of  $\alpha$ . We, thus, finally conclude that within the framework of the polarization–intensity gradient method where the inertial term orientation is approximated with the emission gradient orientation, both  $\Sigma_B$  and  $B$  remain robust estimates.

## Appendix B – $|\delta|$ and $\Sigma_B$ across a Larger Sample

With the goal of adding further evidence to the similarities found in the  $|\delta|$ - and  $\Sigma_B$ -maps (Section 4.2) and the proposed evolutionary scenario (Section 5), we analyze an additional 24 sources from the CSO catalog (Dotson et al. 2010). Sources are chosen based on their coverage of detected polarized emission, together with the condition that the Stokes  $I$  continuum emission need to be strong enough to define a gradient. In order to have at least some connected patches, we request a minimum of 10 measured polarization – intensity gradient pairs.

The Figures 15 to 20 display 4 panels for each source: magnetic field and intensity gradient segments overlaid on Stokes  $I$  dust continuum,  $|\delta|$ -map,  $\Sigma_B$ -map and the  $\Sigma_B$  versus  $|\delta|$  connection. The Figures 21 to 23 show the corresponding magnetic field versus intensity gradient correlations with the histograms for  $|\delta|$ . Basic statistical numbers are summarized in Table 2.

## REFERENCES

- Acord, J.M., Churchwell, E., & Wood, D.O.S. 1998, *ApJ*, 495, 107
- Alves, F.O., Girart, J.M., Lai, S.-P., Rao, R., & Zhang, Q. 2010, *ApJ*, 726, 63
- Anthony-Twarog, B.J. 1982, *AJ*, 87, 1213
- Campbell, M.F., Niles, D., Nawfel, R., Hawrylycz, M., Hoffmann, W.F., & Thronson, H.A., Jr. 1982, *ApJ*, 261, 550
- Carrasco-González, C., Rodríguez, L.F., Anglada, G., Martí, J., Torrelles, J.M., & Osorio, M. 2010, *Science*, 339, 1209C
- Chen, H.-R., Rao, R., Wilner, D.J., & Liu, S.-Y., 2012, *ApJ*, 751L, 13C
- Crutcher, R.M., Hakobian, N., & Troland, T.H. 2009, *ApJ*, 692, 844
- Crutcher, R.M. 2012, *ARAA*, Volume 50, August 18, 2012
- Dotson, J.L., Vaillancourt, J.E., Kirby, L., Dowell, C.D., Hildebrand, R.H., & Davidson, J.A. 2010, *ApJS*, 186, 406
- Draine, B.T., & Weingartner, J.C. 1996, *ApJ*, 470, 551
- Draine, B.T., & Weingartner, J.C. 1997, *ApJ*, 480, 633
- Etoka, S., Gray, M.D., & Fuller, G.A. 2012, *MNRAS*, 423, 647
- Genzel, R., et al. 1981, *ApJ*, 247, 1039
- Genzel, R., Pichon, C., Eckart, A., Gerhard, O.E., & Ott, T. 2000, *MNRAS*, 317, 348
- Girart, J.M., Rao, R., and Marrone, D.P. 2006, *Science*, 313, 812
- Girart, J.M., Beltrán, M. T., Zhang, Q., Rao, R., & Estalella, R. 2009, *Science*, 324, 1408
- Girart, J.M., Patel, N., Vlemmings, W.H.T., & Rao, R. 2012, 751L, 20G
- Girart, J.M., Frau, P., Zhang, Q., Koch, P.M., Qiu, K., Tang, Y.-W., Lai, S.-P., & Ho, P.T.P. 2013, *ApJ*, 772, 69
- Goldreich, P., & Kylafis, N.D. 1981, *ApJ*, 243, 75
- Goldreich, P., & Kylafis, N.D. 1982, *ApJ*, 253, 606

- Gwinn, C.R., Moran, J.M. & Reid, M.J. 1992, *ApJ*, 393, 149
- Hezareh, T., Houde, M., McCoey, C., & Li, H. 2011, arXiv:1007.2242
- Hildebrand, R.H. 1988, *QJRAS*, 29, 327
- Hildebrand, R.H., Kirby, L., Dotson, J.L., Houde, M., & Vaillancourt, J.E. 2009, *ApJ*, 696, 567
- Ho, P.T.P., & Young, L.M. 1996, *ApJ*, 472, 742
- Ho, P.T.P., Moran, J.M., and Lo, K.-Y. 2004, *ApJ*, 616, 1
- Houde, M., Vaillancourt, J.E., Hildebrand, R.H., Chitsazzadeh, S., and Kirby, L. 2009, *ApJ*, 706, 1504
- Houde, M., Rao, R., Vaillancourt, J.E., & Hildebrand, R.H. 2011, *ApJ*, 733, 109
- Hull, C.L.H., Plambeck, R.L., Bolatto, A.D., et al., 2013, *ApJ*, 768, 159
- Immer, K., Reid, M. J., Menten, K. M., Brunthaler, A., & Dame, T. M. 2013, *A&A*, 553, A117
- Keto, E., & Klaassen, P. 2008, *ApJ*, 678, L109
- Kirby, L. 2009, *ApJ*, 694, 1056
- Koch, P.M., Tang, Y.-W., & Ho, P.T.P. 2010, *ApJ*, 721, 815
- Koch, P.M., Tang, Y.-W., & Ho, P.T.P. 2012a, *ApJ*, 747, 79
- Koch, P.M., Tang, Y.-W., & Ho, P.T.P. 2012b, *ApJ*, 747, 80
- Kuchar, T. A., & Bania, T. M. 1994, *ApJ*, 436, 117
- Lazarian, A. 2007, *J.Quant.Spectrosc.Radiat.Transfer*, 106, 225
- Lai, S.-P., Crutcher, R.M., Girart, J.M., & Rao, R. 2002, *ApJ*, 566, 925
- Li, H., & Houde, M. 2008, *ApJ*, 677, 1151
- Mamajek, E.E. 2008, *Astron. Nachr.*, 329, 10
- Matthews, B.C., McPhee, C.A., Fissel, L.M., & Curran, R.L. 2009, *ApJS*, 182, 143
- Menten, K.M., Reid, M.J., Forbrich, J., & Brunthaler, A. 2007, *A&A*, 474, 515
- Padovani, M., Brinch, C., Girart, J.M. et al., 2012, *A&A*, 543A, 16P

- Park, B.-G. & Sung, H. 2002, *AJ*, 123, 892
- Povich, M. S. et al. 2007, *ApJ*, 660, 346
- Racine, R., & van de Bergh, S. 1970, in *IAU Symp.38, The Spiral Structure of Our Galaxy*, ed. W.Becker & Contopoulos (Dordrecht:Reidel), 219
- Rao, R., Girart, J.M., Marrone, D.P., Lai, S.-P., & Schnee, S. 2009, *ApJ*, 707, 921
- Reid, M.J., Menten, K.M., Xheng, X.W., Brunthaler, A., & Xu, Y. 2009, *ApJ*, 705, 1548
- Rodriguez, L.F., Moran, J.M., Ho, P.T.P., & Gottlieb, E.W. 1980, *ApJ*, 235, 845
- Russeil, D., Zavagno, A., Adami, C. et al. 2012, *A&A*, 538, A142
- Shinnaga, H., Novak, G., Vaillancourt, J.E. et al., 2012, *ApJ*, 750, L29
- Sollins, P. K., Zhang, Q., & Ho, P.T.P. 2004, *ApJ*, 606, 943
- Soler, J.D., Hennebelle, P., Martin, P.G., Miville-Deschênes, M.-A., Netterfield, C.B., & Fissel, L.M. 2013, *ApJ*, 774, 128
- Stephens, I.W., Looney, L.W., Kwon, W., et al., *ApJ*, 769L, 15S
- Surcis, G., Vlemmings, W.H.T., Curiel, S., Hutawarakorn Kramer, B., Torrelles, J.M., & Sarma, A.P. 2011, *A&A*, 527A, 48S
- Surcis, G., Vlemmings, W.H.T., van Langevelde, H.J., & Hutawarakorn Kramer, B. 2012, *A&A*, 541A, 47S
- Tang, Y.-W., Ho, P.T.P., Girart, J.M., Rao, R., Koch, P.M., & Lai, S.-P. 2009a, *ApJ*, 695, 1399
- Tang, Y.-W., Ho, P.T.P., Koch, P.M., Girart, J.M., Lai, S.-P., & Rao, R. 2009b, *ApJ*, 700, 251
- Tang, Y.-W., Ho, P.T.P., Koch, P.M., & Rao, R. 2010, *ApJ*, 717, 1262
- Tang, Y.-W., Ho, P.T.P., Koch, P.M., Guilloteau, S., & Dutrey, A. 2013, *ApJ*, 763, 135
- Tassis, K., Dowel, C.D., Hildebrand, R.H., Kirby, L., & Vaillancourt, J.E. 2009, *MNRAS*, 399, 1681
- Vaillancourt, J.E., Dowell, C.D., Hildebrand, R.H. et al., 2008, *ApJ*, 697L, 25V
- Vaillancourt, J.E., & Matthews, B.C. 2012 *ApJ*, 201, 13V
- Vlemmings, W.H.T., Humphreys, E.M.L., & Franco-Hernández, R. 2011, *ApJ*, 728, 149



- Vlemmings, W.H.T., Ramstedt, S., Rao, R., & Maercker, M. 2012, A&A, 540, L3
- Walker, M.F. 1956, ApJS, 2, 365
- Xu, Y., Reid, M.J., Zheng, X.W., & Menten, K.M. 2006, Science, 311, 54
- Young, L. M., Keto, E., & Ho, P.T.P. 1998, ApJ, 507, 270
- Zhang, Q., & Ho, P.T.P. 1997, ApJ, 488, 241
- Zhang, Q., Ho, P.T.P., & Ohashi, N. 1998, ApJ, 494, 636

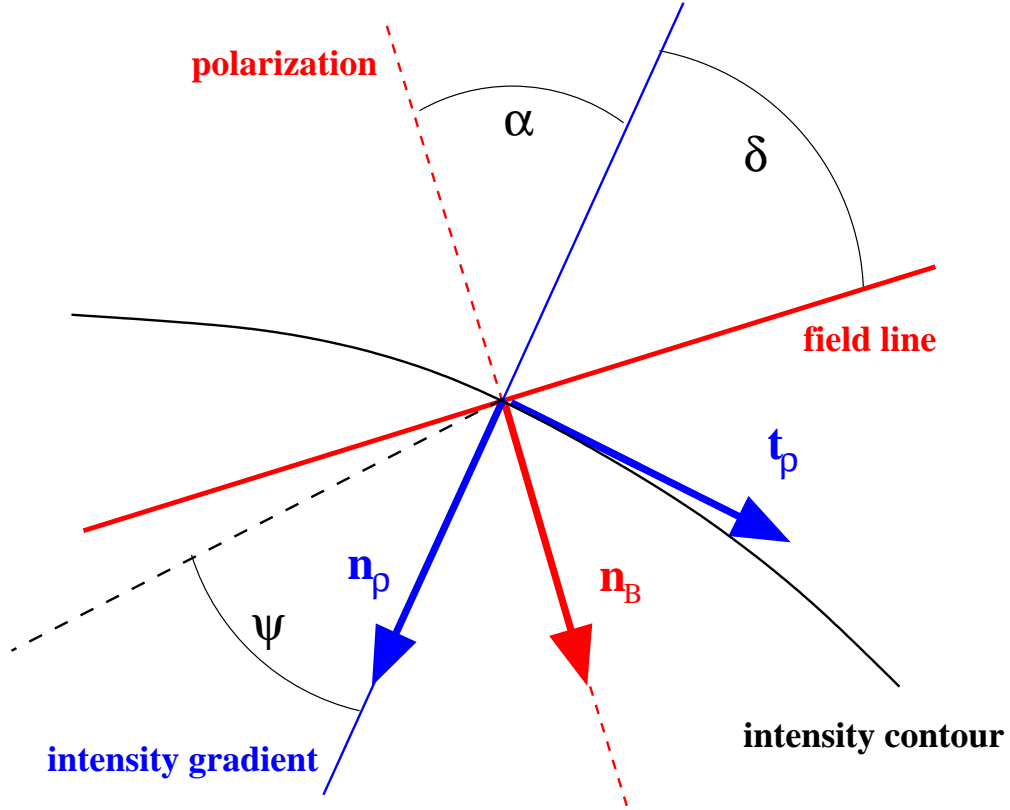


Fig. 1.— The angle  $\delta$  between magnetic field orientation (red solid line) and intensity gradient orientation (blue solid line). The magnetic field tension force is directed normal to the field line along the unity vector  $\mathbf{n}_B$  which is collinear to the originally detected dust polarization orientation (red dashed line). The unity vector  $\mathbf{n}_\rho \equiv \frac{\nabla \rho}{|\nabla \rho|}$  is normal to the emission intensity contour (black solid line) which leads to  $\mathbf{n}_B \cdot \mathbf{n}_\rho = \cos \alpha = \sin \delta$  with  $\delta + \alpha = \pi/2$ . The unity vector  $\mathbf{t}_\rho$  is tangential to the emission contour, forming an orthonormal system together with  $\mathbf{n}_\rho$ . The deviation between intensity gradient and gravity and/or pressure gradient orientations (black dashed line) is indicated with the angle  $\psi$ .

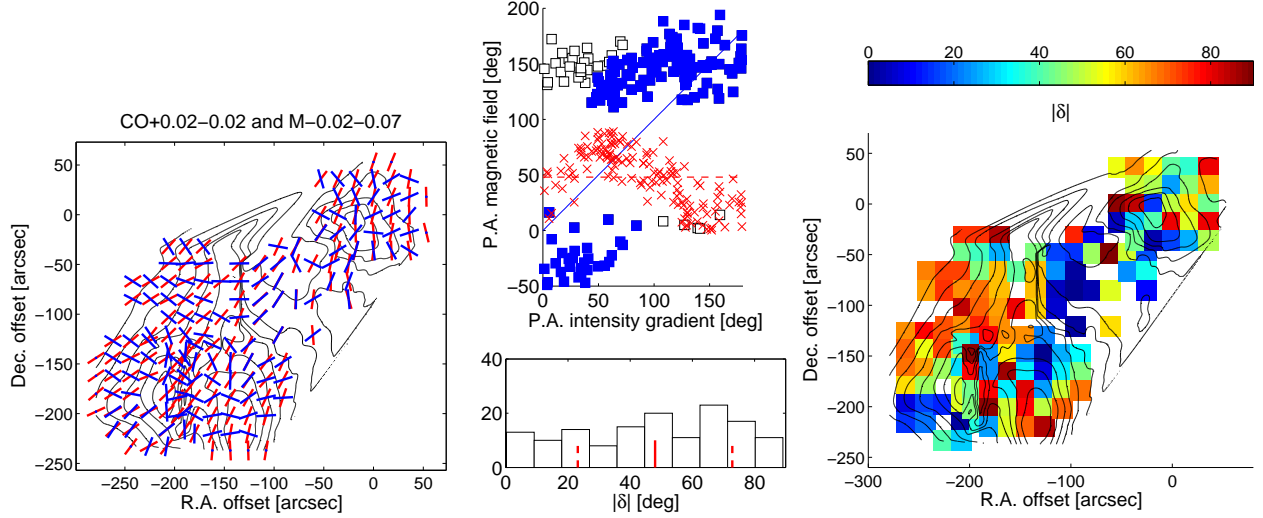


Fig. 2.— The complex CO+0.02–0.02 together with M–0.02–0.07 (CSO, Dotson et al. (2010)). The left panel shows the dust Stokes  $I$  continuum contours, overlaid with the magnetic field segments (red) and the intensity gradient segments (blue). The right panel displays the absolute difference,  $|\delta|$ , between the 2 orientations in the range from  $0^\circ$  to  $90^\circ$ . The correlation between the magnetic field and intensity gradient orientations is illustrated with the blue filled squares in the middle top panel. The black empty squares belong to pairs with  $P.A.s$  close to  $P.A. = 0$ , one  $P.A.$  being on the left and the other being on the right hand side of the vertical. In order to properly display their correlations, the magnetic field  $P.A.$  is re-defined beyond the  $0$  to  $180^\circ$  range for these cases (blue filled squares above  $180^\circ$  and below  $0^\circ$ ). For visual guidance added is the straight blue line, representing a perfect correlation. Also shown are the absolute differences ( $\leq 90^\circ$ ) between the  $P.A.s$  for each pair (red crosses). Both  $P.A.s$  are defined counter-clockwise starting from north. The red dashed line marks the average absolute difference  $\langle |\delta| \rangle$ . Errors in the magnetic field  $P.A.s$  are typically a few degrees, with maximum uncertainties up to about  $10^\circ$  (not shown). Uncertainties in the intensity gradient  $P.A.s$  are limited to a few degrees after averaging and interpolating Stokes  $I$  values. Resulting errors in  $|\delta|$  then range from a few degrees up to a maximum of about  $10^\circ$ . The histogram in the middle bottom panel represents the distribution of  $|\delta|$  with its mean and  $\pm$ -standard deviation marked with the red solid and dashed lines.

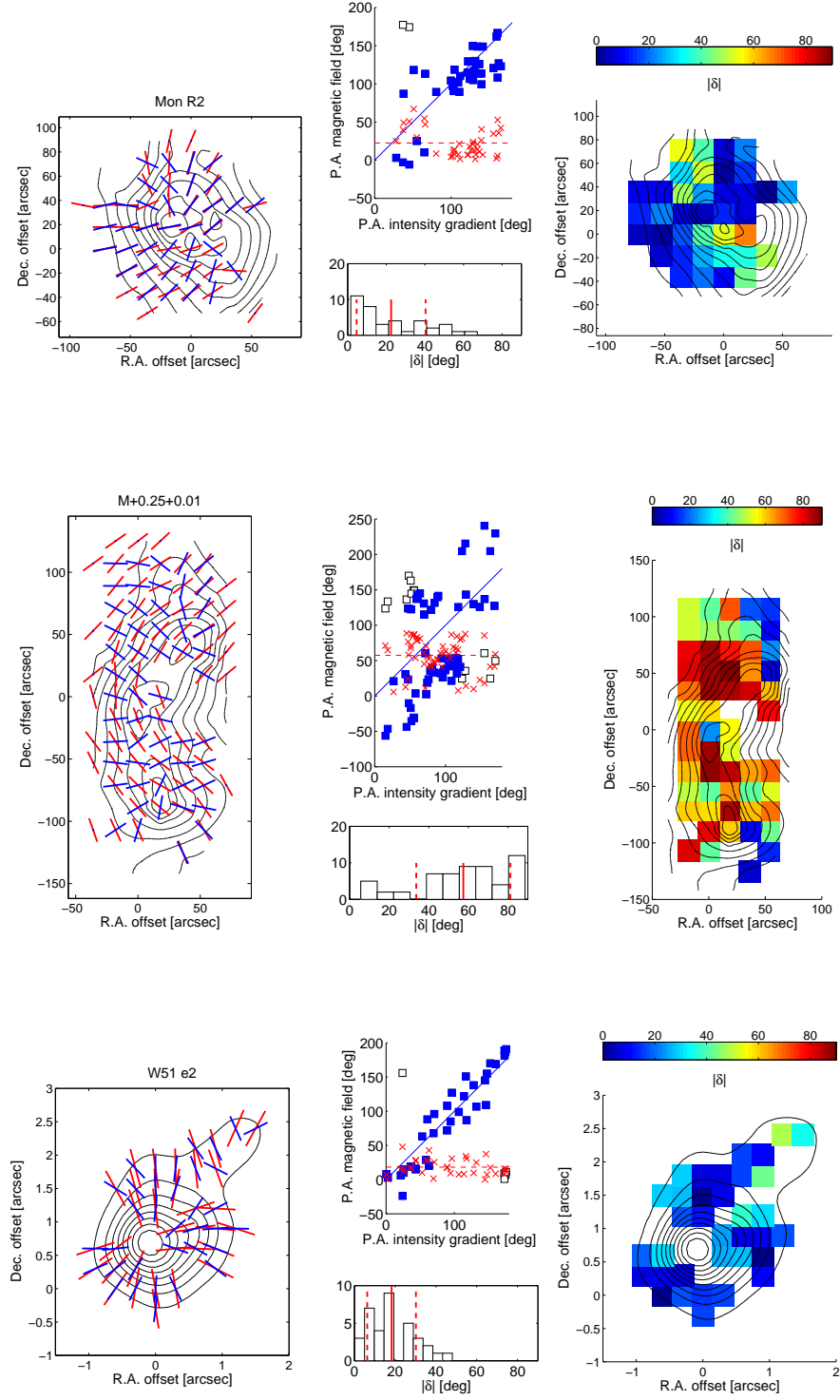


Fig. 3.— The same as in Figure 2 but for the sources Mon R2 and M+0.25+0.01 (CSO, Dotson et al. (2010)) and W51 e2 (Tang et al. 2009b) from top to bottom. For completeness, left panel and histogram for W51 e2 are reproduced from Koch, Tang & Ho (2012a). The error estimate for  $|\delta|$  in these sources is identical to the one for Figure 2.

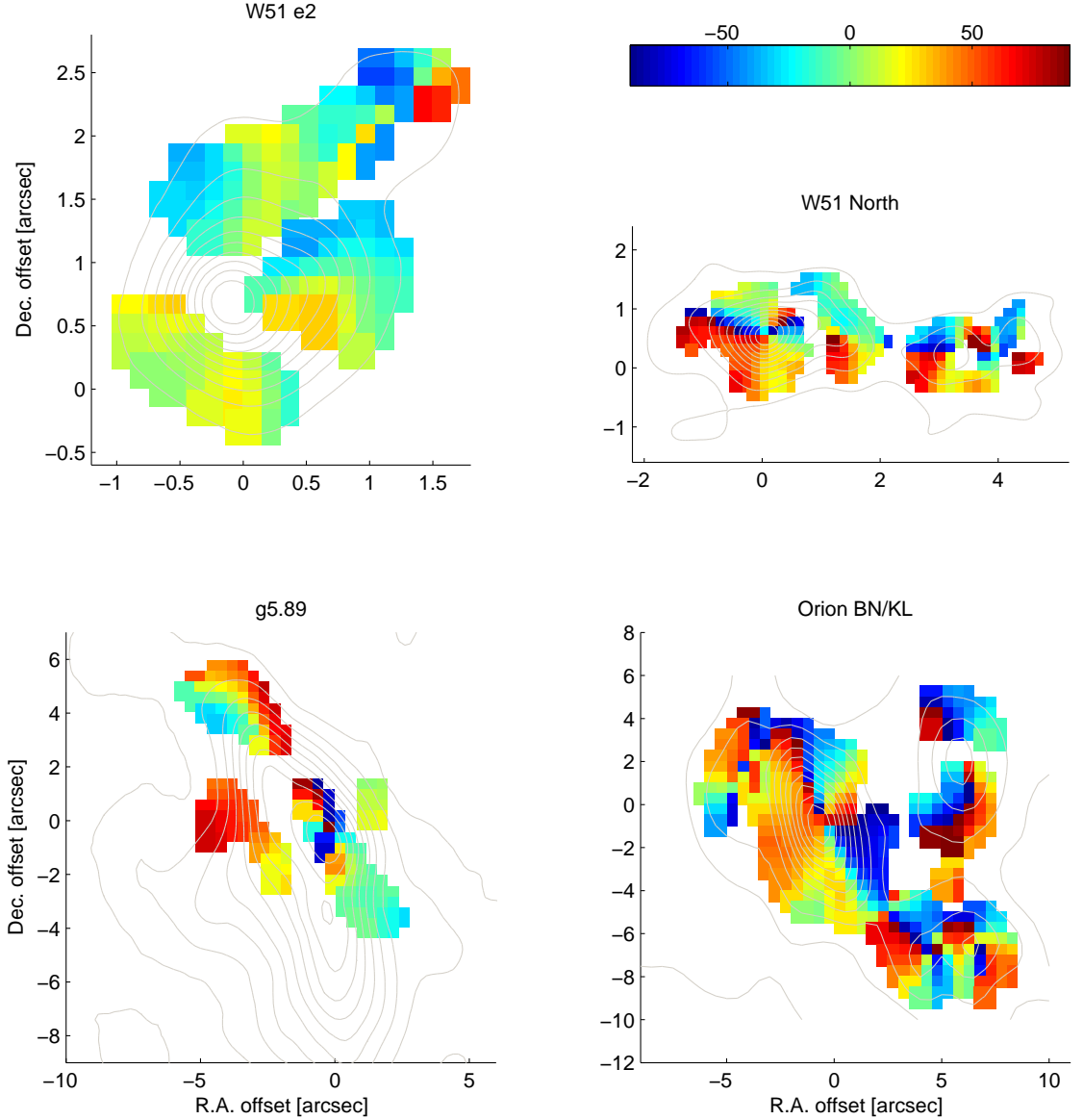


Fig. 4.— Relative difference maps ( $-90^\circ \leq \delta \leq 90^\circ$ ) for the sources W51 e2, W51 North, g5.89 and Orion BN/KL. Colors correspond to the color wedge on the top with units in deg. For an enhanced visual impression, the data are over-gridded to about  $0.15''$  for W51 North and e2,  $0.4''$  for g5.89 and  $0.5''$  for Orion BN/KL, which is about 5 times their synthesized beam resolutions (Table 2). Overlaid are contours of the Stokes  $I$  dust continuum emission. Original maps with magnetic field segments are in Tang et al. (2013), Tang et al. (2010) and Tang et al. (2009a) for W51 North, Orion BN/KL and g5.89, respectively.

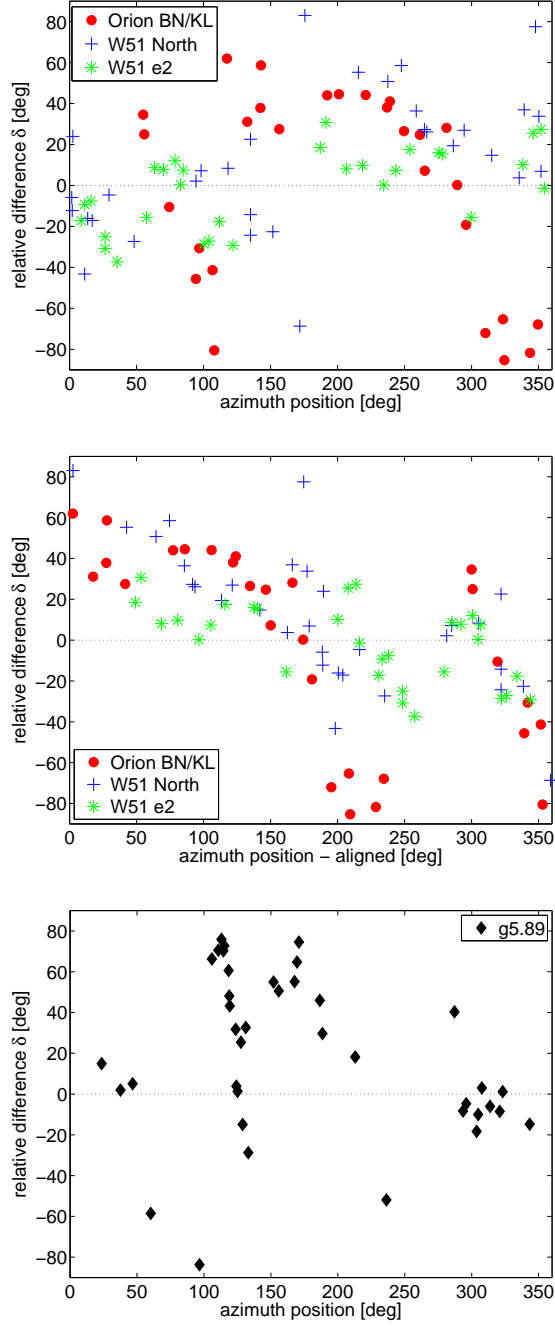


Fig. 5.— Relative difference ( $-90^\circ \leq \delta \leq 90^\circ$ ) for the sources W51 e2, W51 North (main core in the East), Orion BN/KL (main core in the East) and g5.89 as a function of azimuth. Top panel: azimuth is with respect to the original maps, i.e. measured counter-clockwise starting from west (W51 e2, W51 North and Orion BN/KL). For W51 e2, the 6 segments in the north-western extension where a possibly new core is forming (bottom left panel in Figure 3), are excluded. Middle panel: azimuth coordinates are shifted to maximally align features. With respect to the top panel, the shifts are  $-115^\circ$ ,  $-173^\circ$ ,  $-138^\circ$  for Orion BN/KL, W51 North and W51 e2, respectively. Bottom panel: for comparison displayed is g5.89 which shows much less pronounced azimuth features in  $\delta$ . Unlike in Figure 4, only the originally detected non-over-gridded data are displayed here.

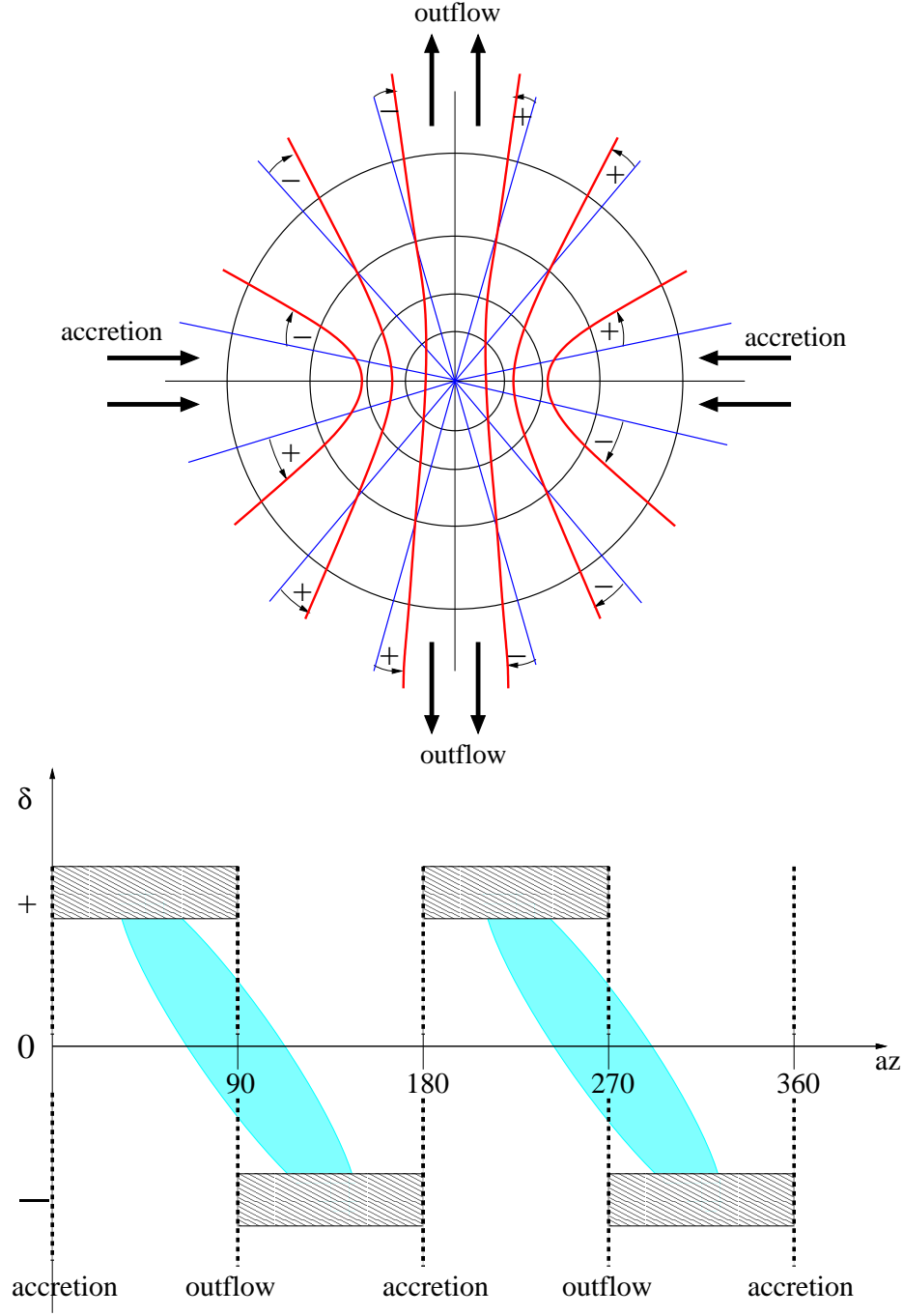


Fig. 6.— Top panel: Schematic illustration of the relative difference ( $-90^\circ \leq \delta \leq 90^\circ$ ) as a function of azimuth for a prototype collapsing core with pinched magnetic field lines. Magnetic field lines are shown with red solid lines. For simplicity circular intensity emission contours (black solid lines) with radial intensity emission gradients (solid blue lines) are assumed. Expected accretion and outflow directions are indicated with arrows. Bottom panel:  $\delta$  as a function of azimuth, measured from the west in the top panel. The quadrants where  $\delta$  is negative or positive are indicated with the hatched areas. The areas in cyan indicate the continuous change in  $\delta$  across zero in the outflow areas (around azimuth 90 and 270), and the more abrupt change with a flip in sign across the accretion zones (azimuth 0 and 180). Note that a flattened ellipsoidal structure in the top panel will still leave these characteristic zones unchanged. The above schematics can also explain the bimodal distribution in  $\delta$  around 0, which was first clearly observed for W51 e2 in Figure 2 in Koch, Tang & Ho (2012a).  $\delta$ -distributions for all sources are shown in Figure 7.

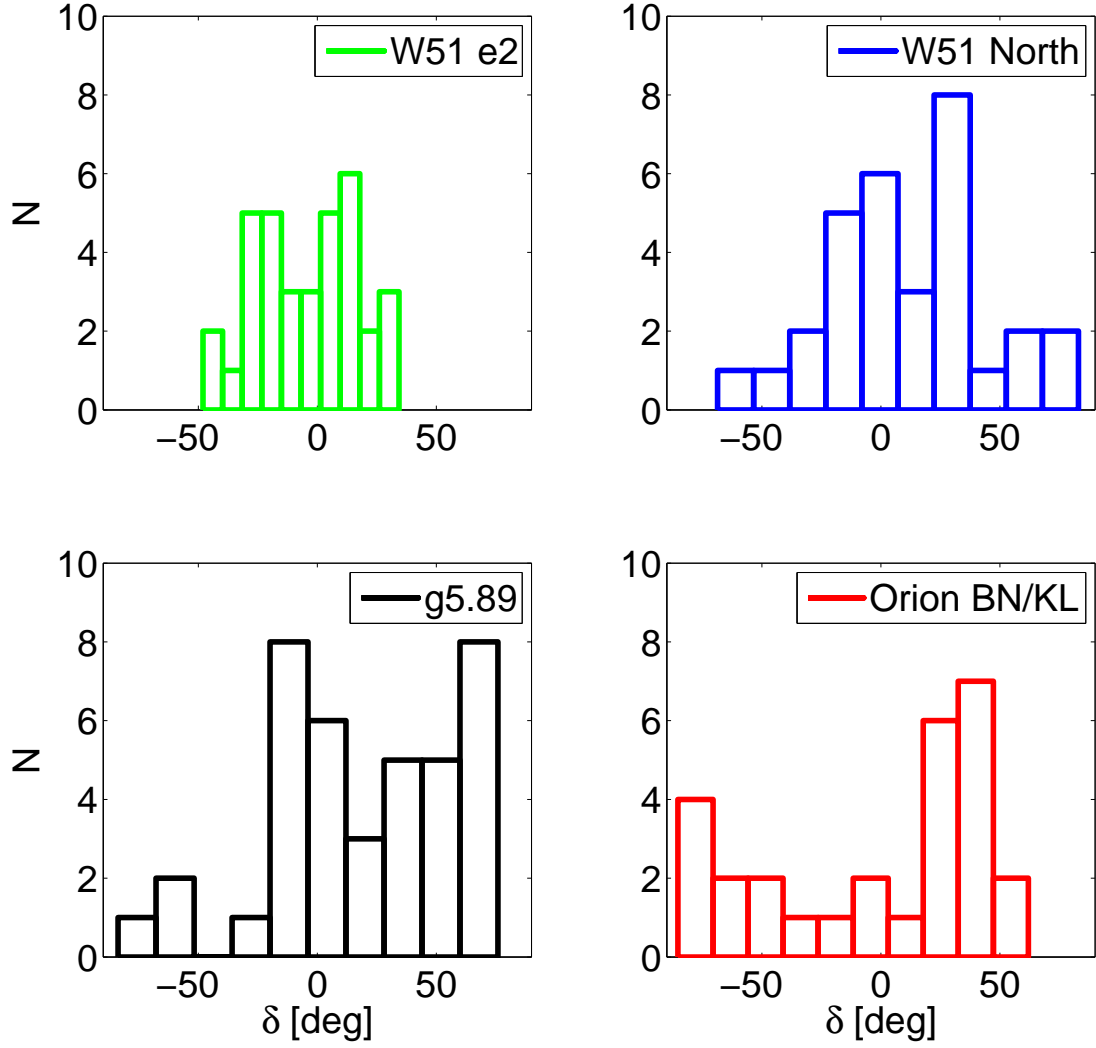


Fig. 7.— Distributions of the relative-difference angles  $\delta$  as displayed in Figure 5 for W51 e2, W51 North main core, g5.89 and Orion BN/KL main core. Distributions are clearly non-Gaussian. Bimodal distributions are apparent even in the case of g5.89.



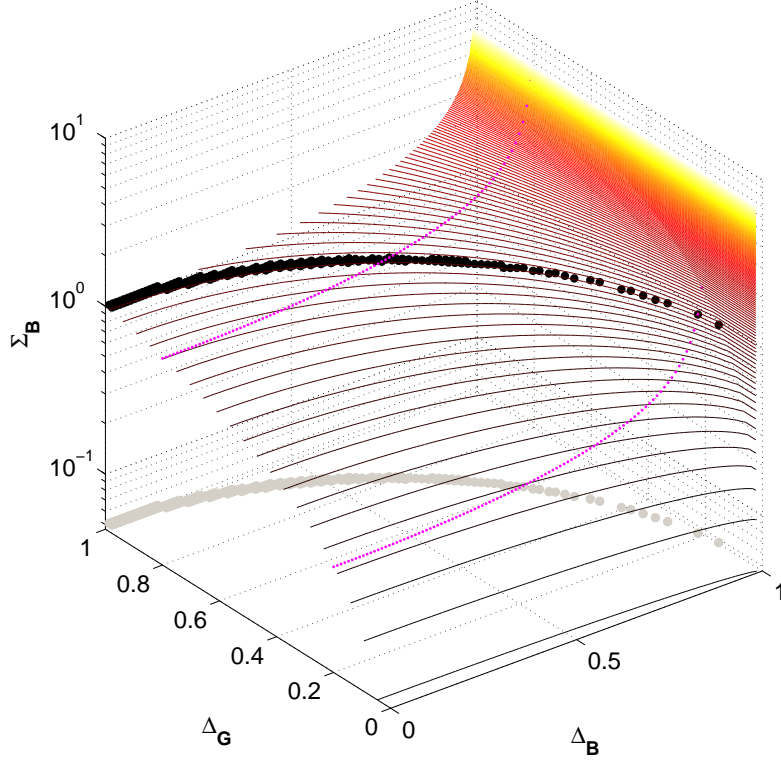


Fig. 8.— The field significance  $\Sigma_B$  as a function of the field and gravity deviations  $\Delta_B$  and  $\Delta_G$ . The gray-dotted line in the  $(\Delta_G, \Delta_B)$ -plane separates the parameter space into  $\Sigma_B < 1$  and  $\Sigma_B > 1$ . The corresponding black-dotted contour line marks  $\Sigma_B \equiv 1$ . The 2 magenta lines are illustrating  $\Sigma_B$  as a function of  $\Delta_B$  for constant  $\Delta_G$ -values. At the boundary  $\Delta_B \equiv 1$  (except for  $\Delta_B = 1$  with  $\Delta_G = 0$ ),  $\Sigma_B$  is, strictly speaking, not defined as the polarization-intensity gradient method (Koch, Tang & Ho 2012a) is failing here.

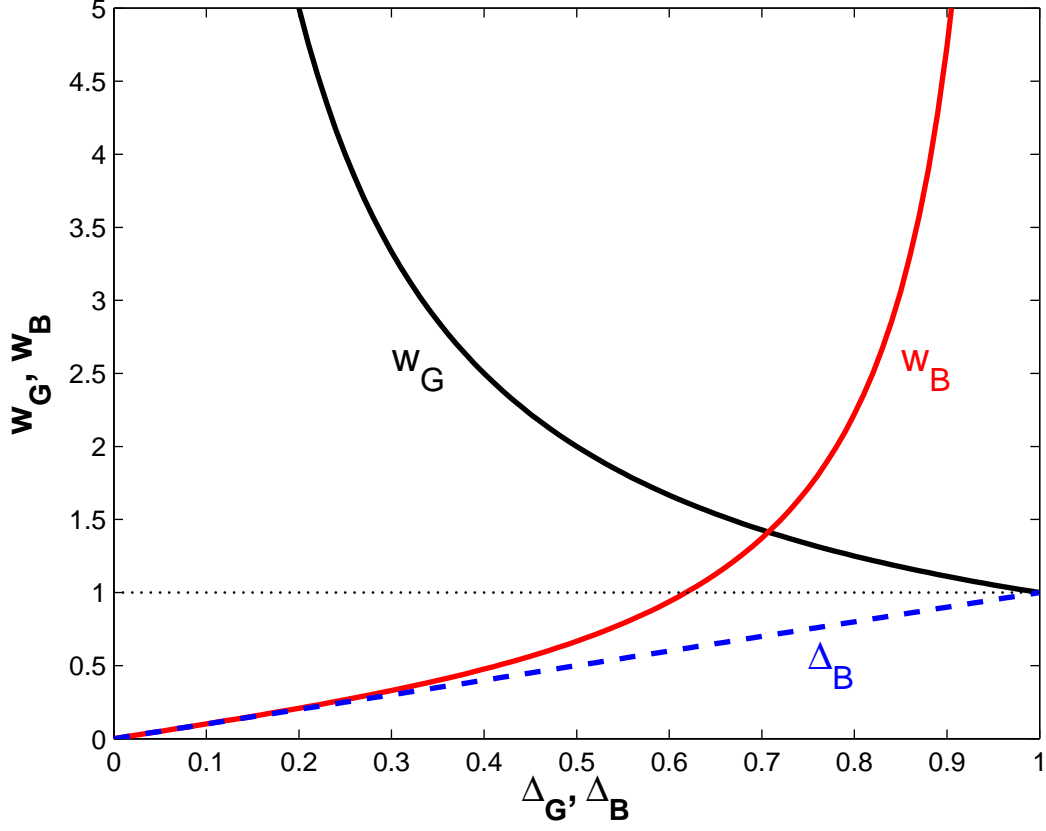


Fig. 9.— The weight functions  $w_B$  and  $w_G$  for the magnetic field and gravity, respectively. The lower limit,  $\Delta_B = \sin|\delta|$ , to the magnetic field weight  $w_B$  is indicated with the blue dashed line. This lower limit is directly obtainable from a  $|\delta|$ -map.  $w_B$  is unity at  $\Delta_B \equiv \Delta_G = 0.618$ , which corresponds to a misalignment of about  $38^\circ$ . Magnetic field and gravity have equal weight at  $\Delta_B \equiv \Delta_G = 0.707$ , i.e.  $45^\circ$ .

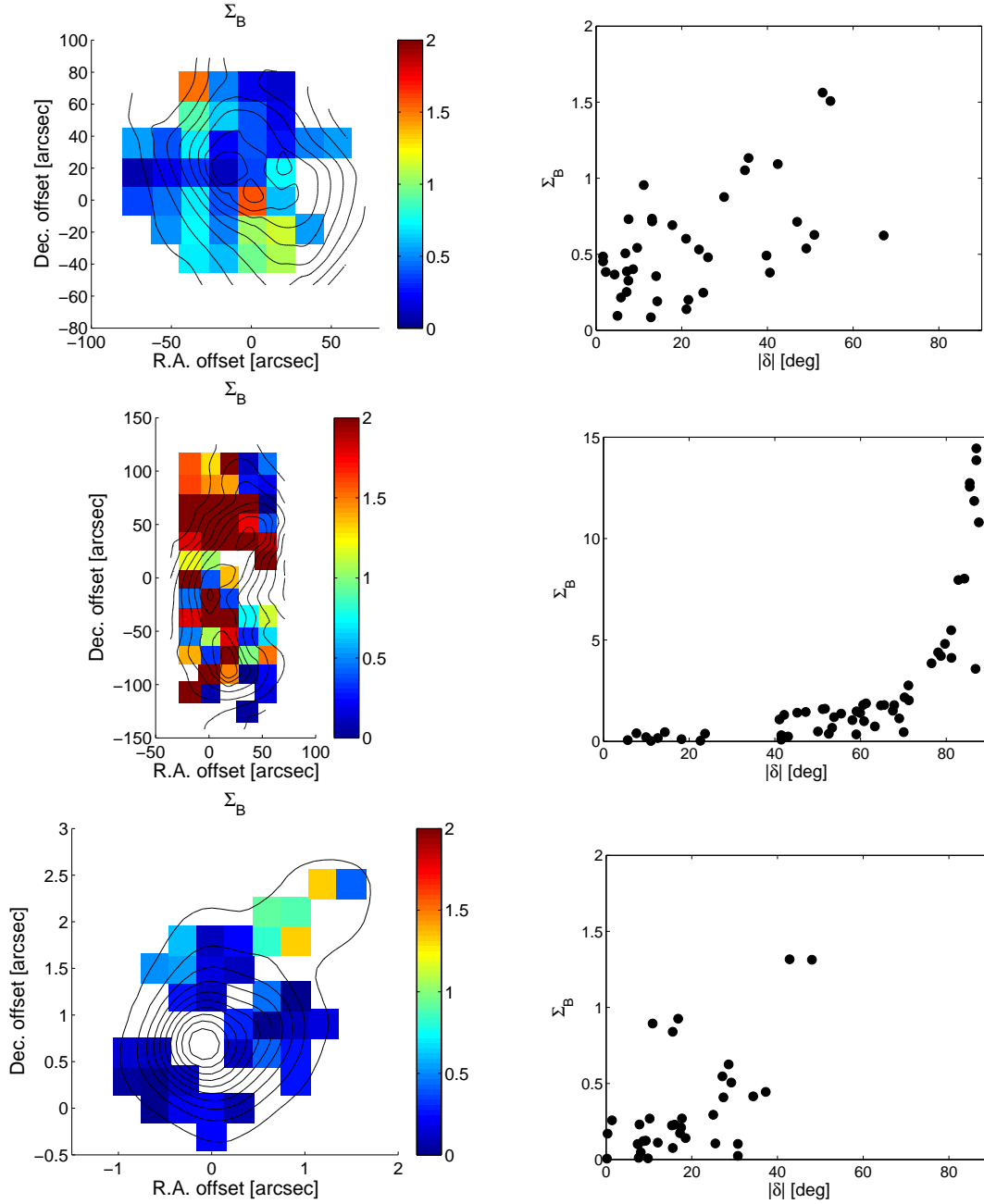


Fig. 10.— Field significance  $\Sigma_B$ -maps (left panels) and  $\Sigma_B$  versus  $|\delta|$  correlation (right panels). From top to bottom shown are the sources Mon R2 and M+0.25+0.01 (CSO, Dotson et al. (2010)) and W51 e2 (Tang et al. 2009b). The exponential-like trend for M+0.25+0.01 results from large  $|\delta|$ -values (small  $\alpha$ -values) which boost the contribution of  $1/\sin \alpha$  in  $\Sigma_B$ . Uncertainties in  $|\delta|$  are a few degrees up to a maximum of about  $10^\circ$ . Errors in  $\Sigma_B$  are in the range of 10 to 20%. They do, thus, not significantly alter the correlation.

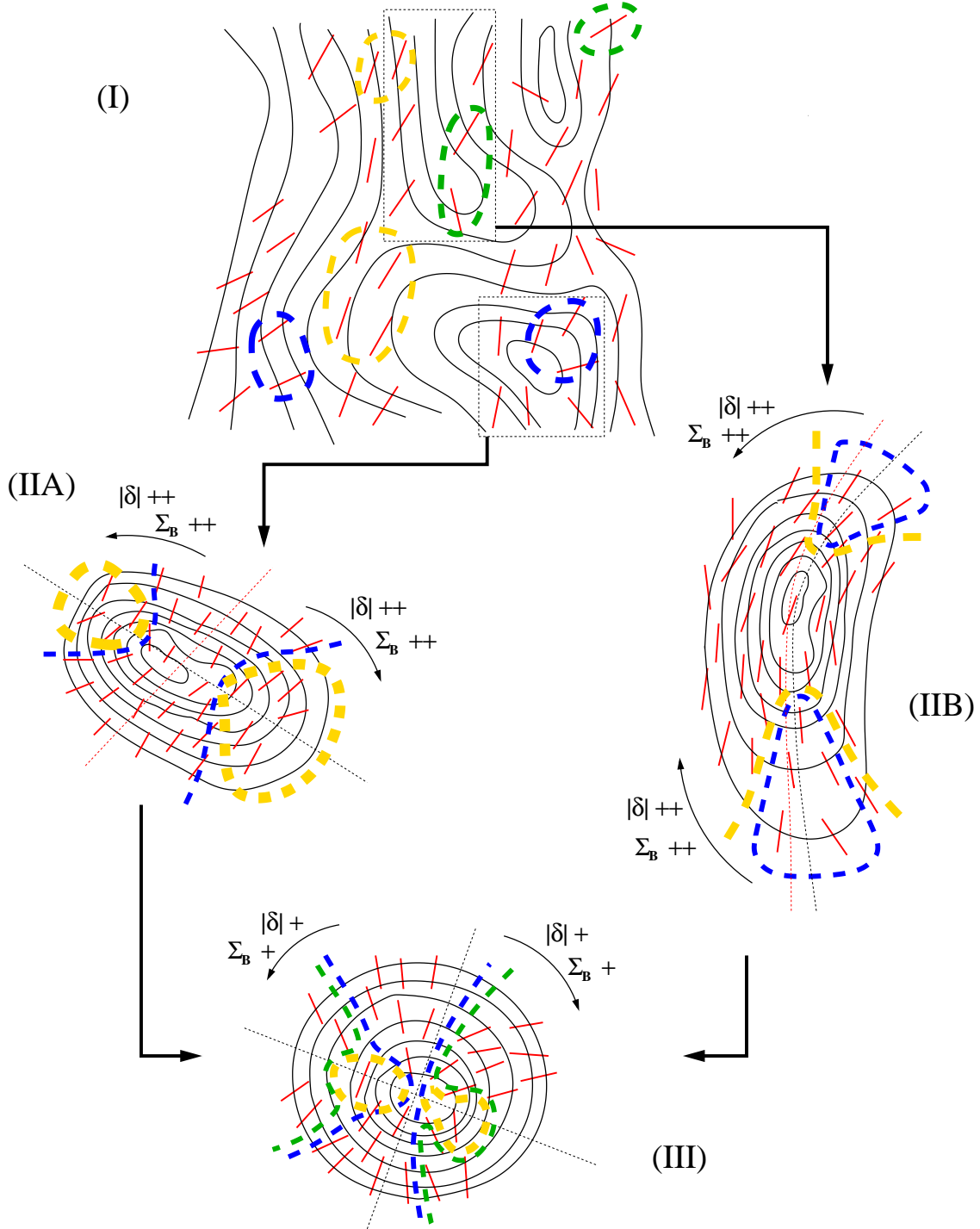


Fig. 11.— Schematic illustration of the angle  $|\delta|$  across an evolutionary sequence in 3 phases as described in Section 5 and summarized in Table 3. The red segments indicate the magnetic field orientations. The black dotted squares in (I) mark the precursor regions for (IIA) and (IIB). Following the color coding used in the Figures 2 and 3 for  $|\delta|$ , blue dashed areas mark regions with close alignment between field and intensity gradient orientations. Yellow areas mark zones with large deviations. Green areas are in between. Mean field orientations (red dotted lines) and dust emission major axis (black dotted lines) are shown in (IIA) and (IIB). Accretion and outflow orientations are shown with black dotted lines in (III), following the interpretation in Section 2.1.2. Arrows with  $|\delta|++$  ( $\Sigma_B++$ ) and  $|\delta|+$  ( $\Sigma_B+$ ) indicate directions of significant and moderate increase in  $|\delta|$  ( $\Sigma_B$ ).

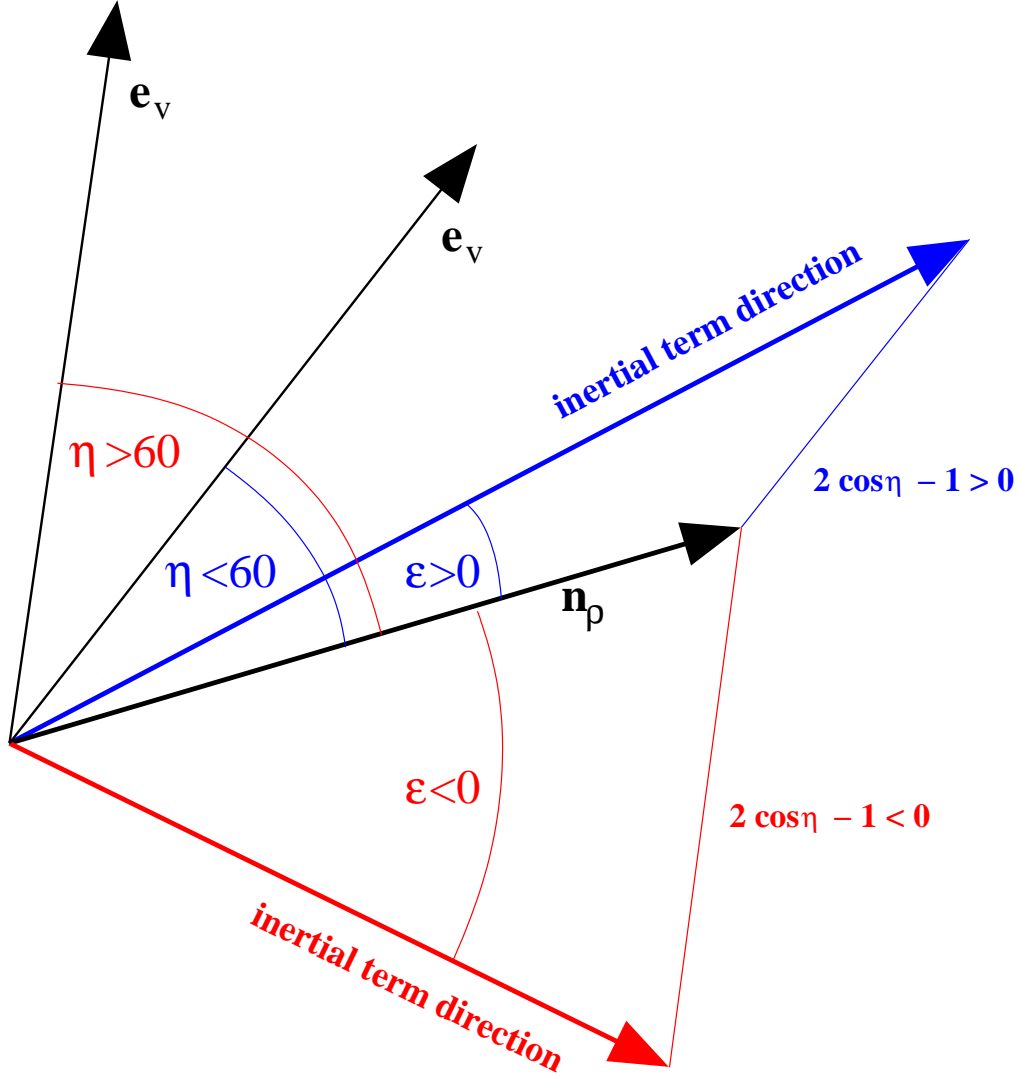


Fig. 12.— Schematic illustration of the inertial term deviation  $\epsilon$ . The angle between the density gradient direction  $\mathbf{n}_\rho$  and the velocity direction  $\mathbf{e}_v$  is labeled with  $\eta$ . Following Equation (10), two cases need to be distinguished where  $\eta \leq 60^\circ$  (illustrated in blue) or  $\eta > 60^\circ$  (in red). The resulting inertial term direction deviates from  $\mathbf{n}_\rho$  by  $\epsilon > 0$  (blue) or  $\epsilon < 0$  (red).

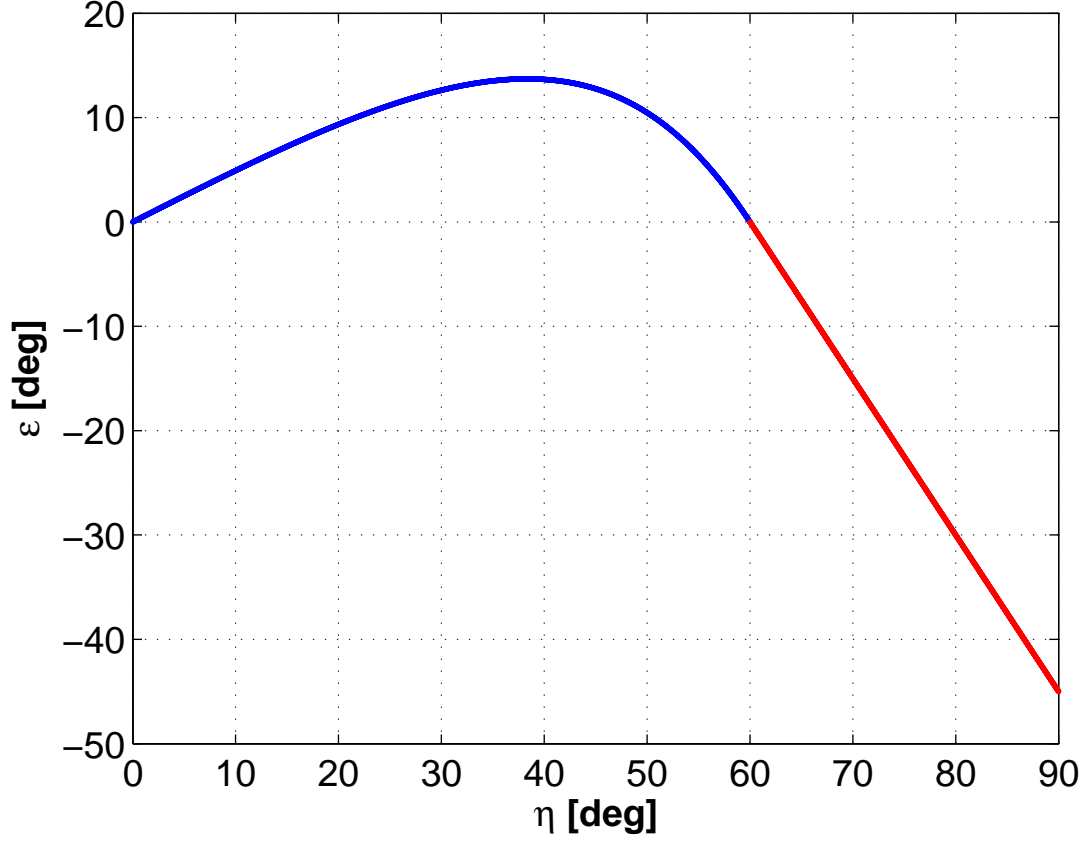


Fig. 13.— Inertial term deviation  $\epsilon$  as a function of the angle  $\eta$  between the density gradient and the velocity direction (Figure 12).  $\epsilon = 0$  indicates that the inertial term is aligned with the density gradient. For angles  $\eta < 60^\circ$  the velocity contribution along  $\mathbf{e}_v$  is added to  $\mathbf{n}_p$  and the deviation  $\epsilon$  is positive (blue regime) with a maximum around  $14^\circ$  and an average deviation of about  $8.8^\circ$ . For angles  $\eta$  larger than  $60^\circ$  the deviation becomes negative because  $\mathbf{e}_v$  is subtracted (red regime).

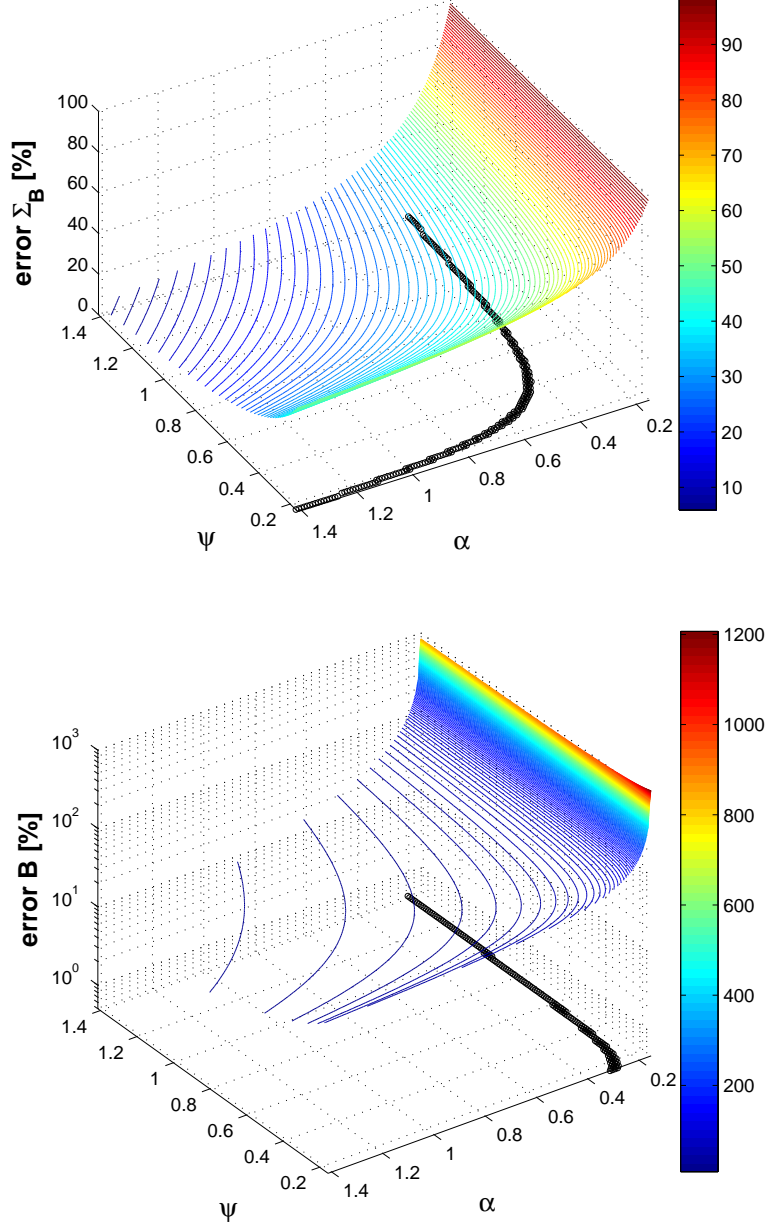


Fig. 14.— Top panel: Errors in the force ratio  $\Sigma_B$  for an average inertial term deviation of  $8.8^\circ$  (Figure 13) as a function of the angles  $\alpha$  and  $\psi$ . The color coding displays the errors in percentage. The black-dotted line in the  $(\alpha, \psi)$ -plane marks the 50 % error boundary. Bottom panel: Errors in the magnetic field strength  $B$  for an average inertial term deviation of  $8.8^\circ$ . The black-dotted line again marks the 50% error boundary.

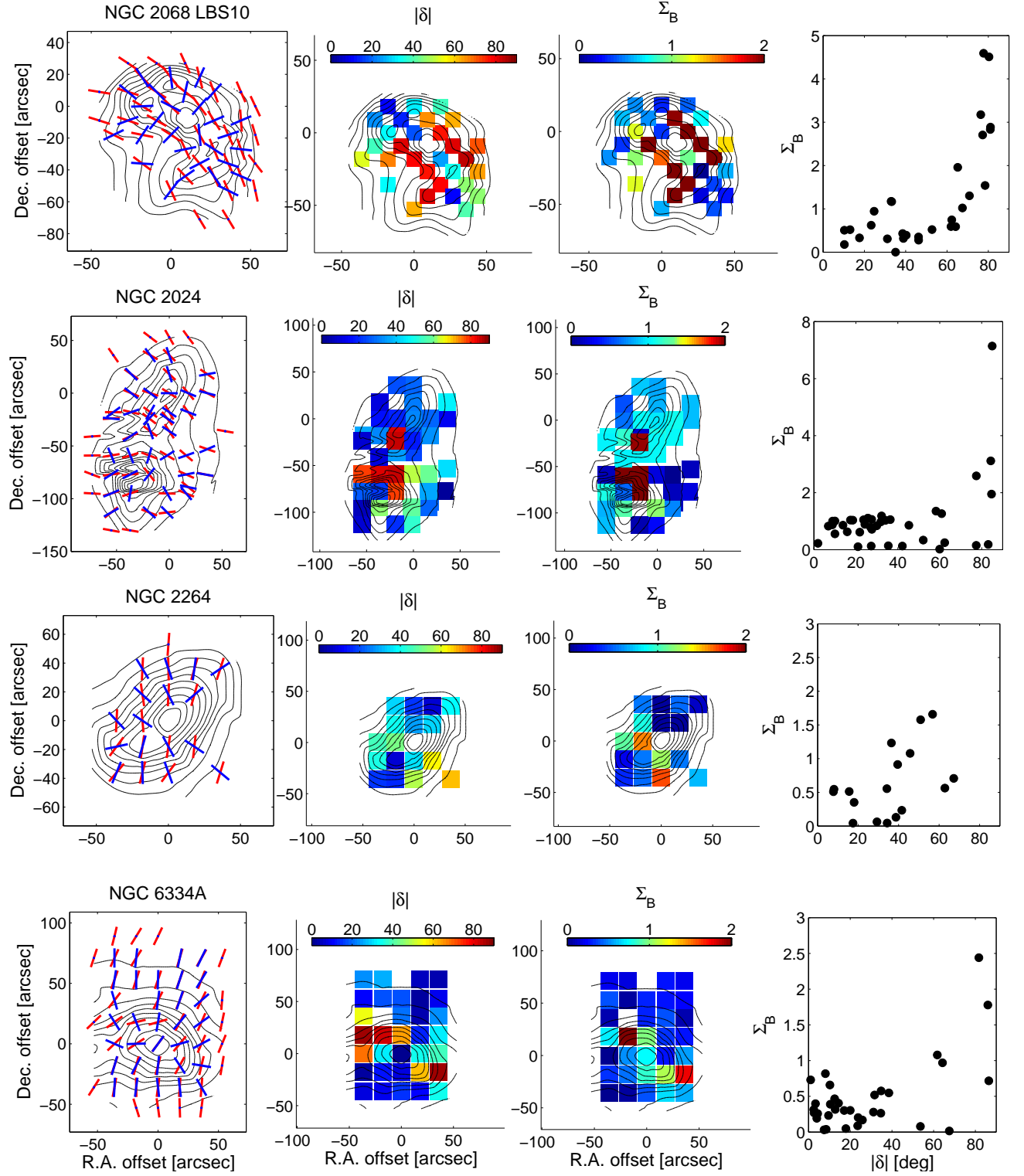


Fig. 15.— Additional sources from the CSO sample (Dotson et al. 2010). The panels from left to right display the Stokes  $I$  dust continuum overlaid with magnetic field segments (red) and dust intensity gradients (blue),  $|\delta|$ -map,  $\Sigma_B$ -map and the connection between  $\Sigma_B$  and  $|\delta|$ . Note that, for a better uniform display across the sample, the color-coding for  $\Sigma_B$  in the third-column panels is saturated at 2.



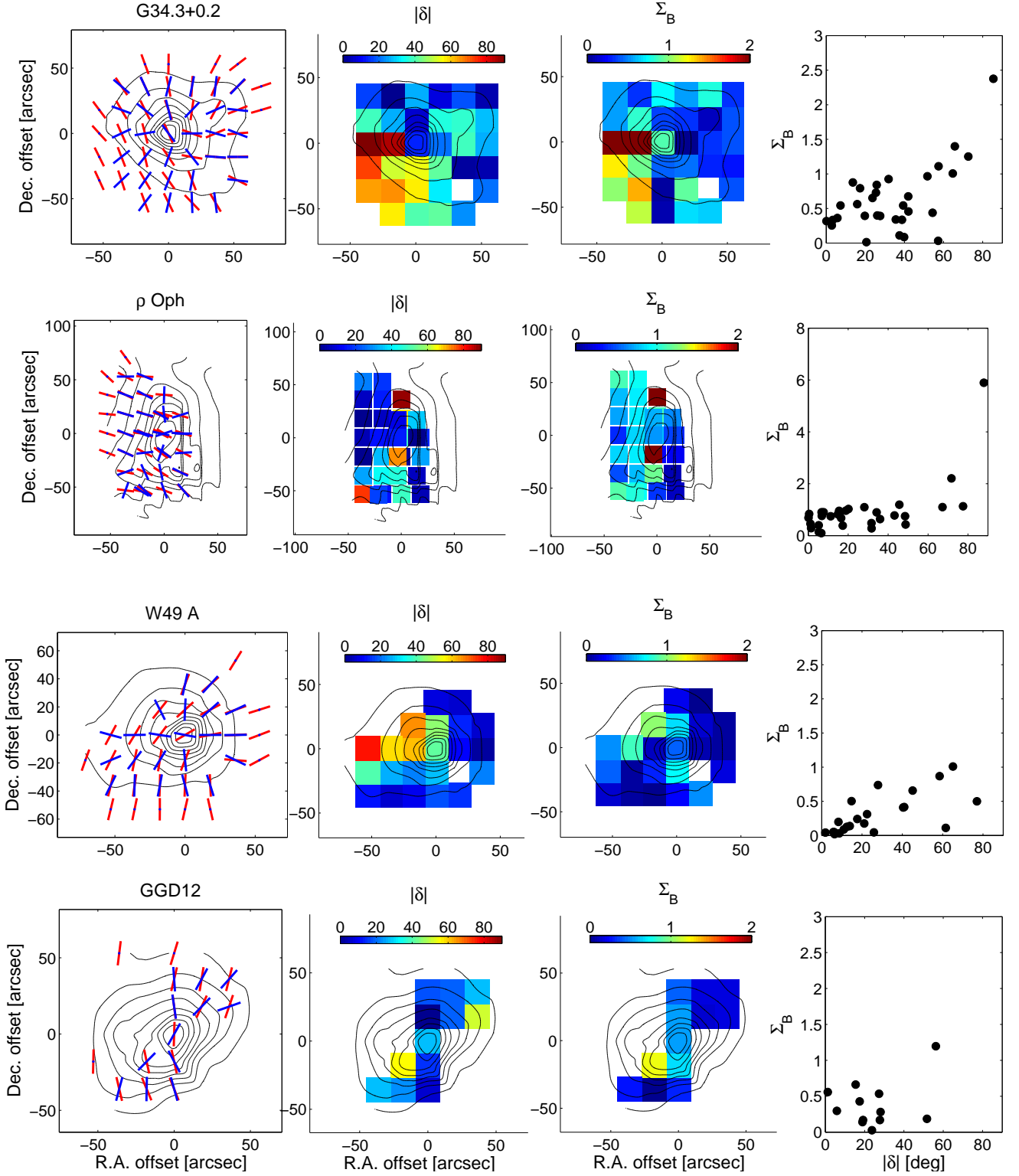


Fig. 16.— Same as in Figure 15.

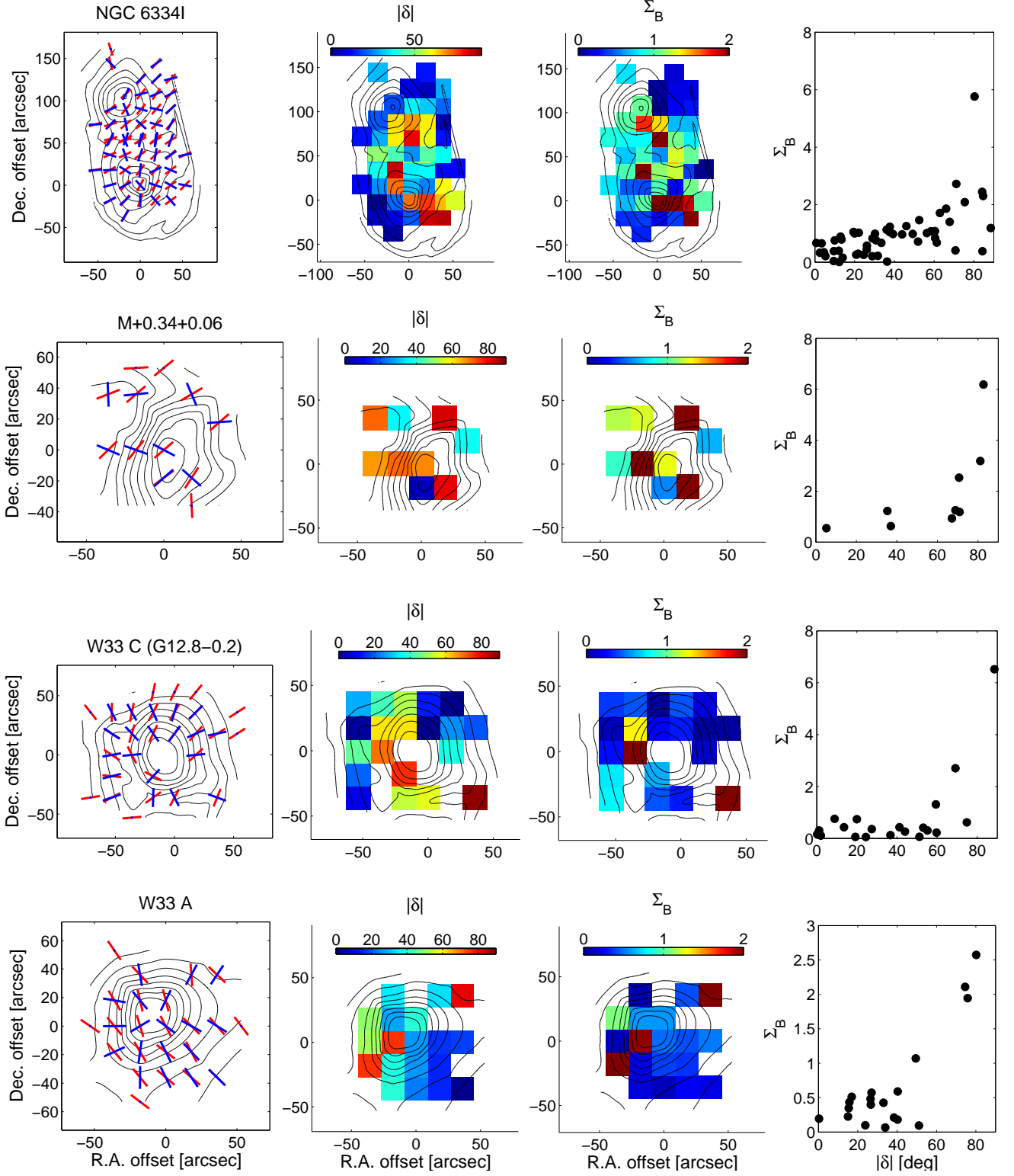


Fig. 17.— Same as in Figure 15.

Table 1. Magnetic Field Quantities

Quantity	Input	Range	Projection Effect?	Modeling?	Information
$\Delta_B$	$\delta$	$[0, 1]$	possible	none: $\delta$ directly measurable	local field efficiency
$\Sigma_B$	$\alpha, \psi$	$[0, \infty]$	none or small	yes: angle $\psi$	relative local field-to-gravity/pressure force
$B$	$\alpha, \psi, \rho, \text{mass}$	$[0, \infty]$	none or small	yes: angle $\psi, \rho, \text{mass}$	absolute local field strength

Note. — Magnetic field quantities in increasing order of complexity and information as discussed in Section 3.

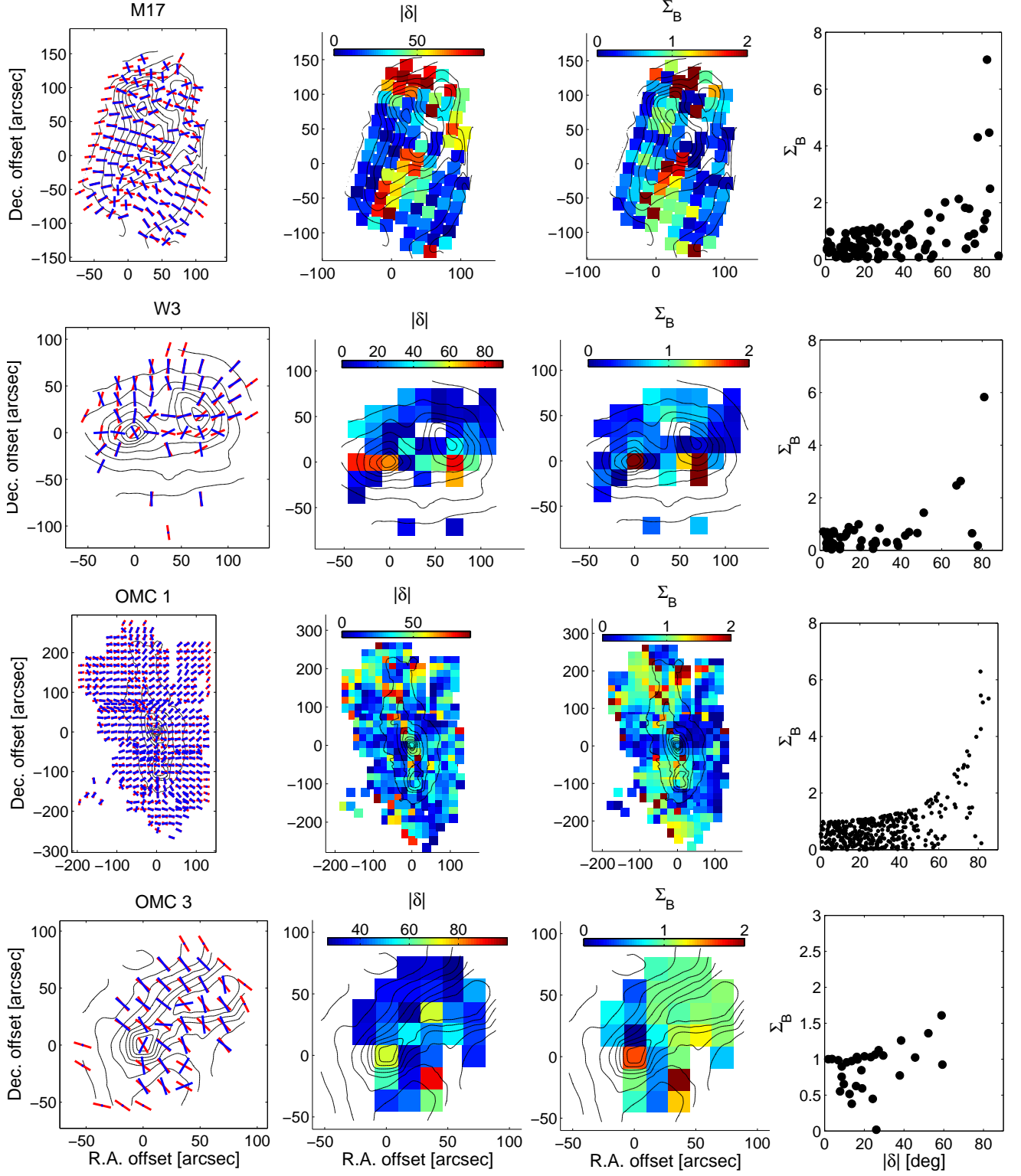


Fig. 18.— Same as in Figure 15.

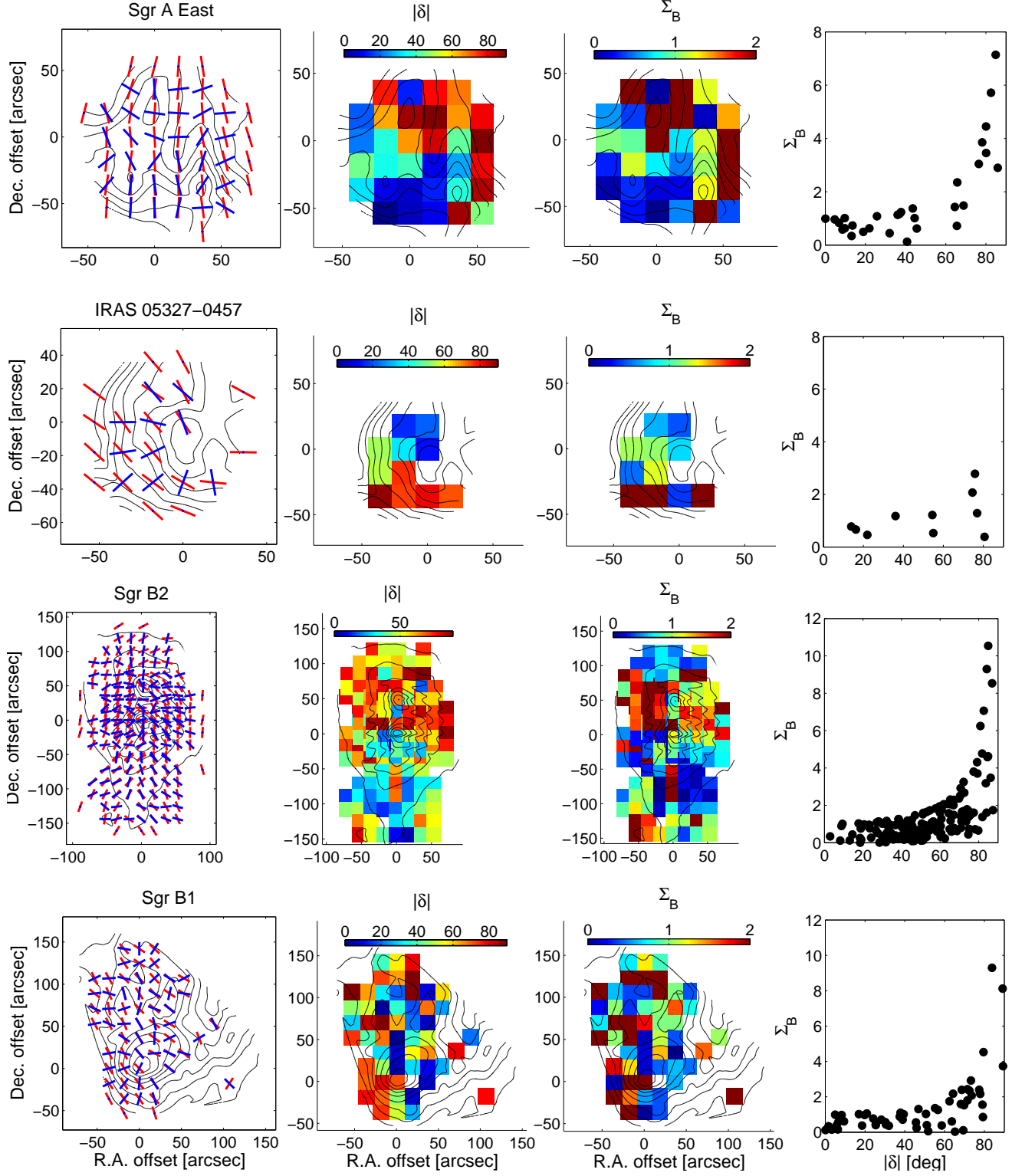


Fig. 19.— Same as in Figure 15.

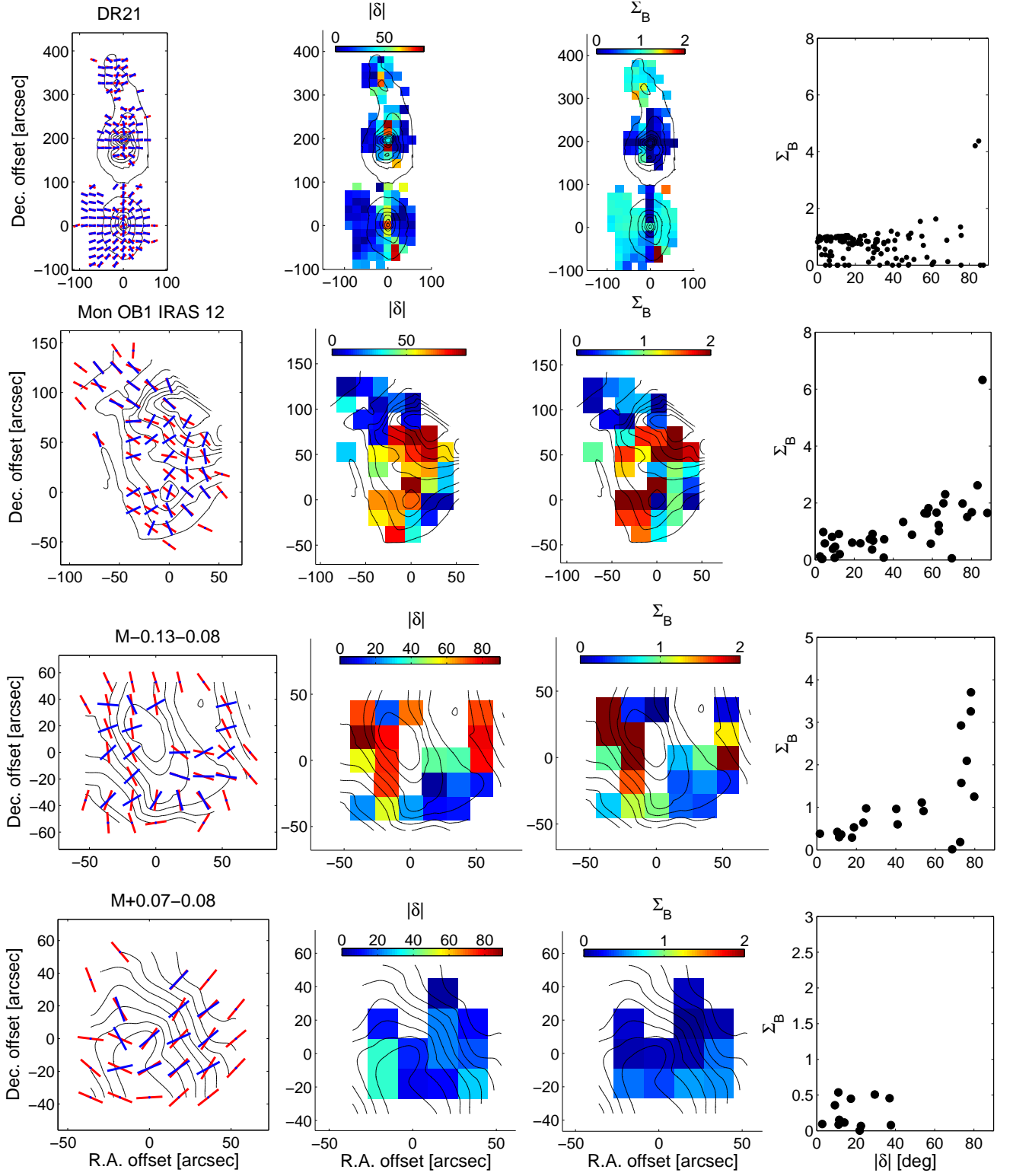


Fig. 20.— Same as in Figure 15.

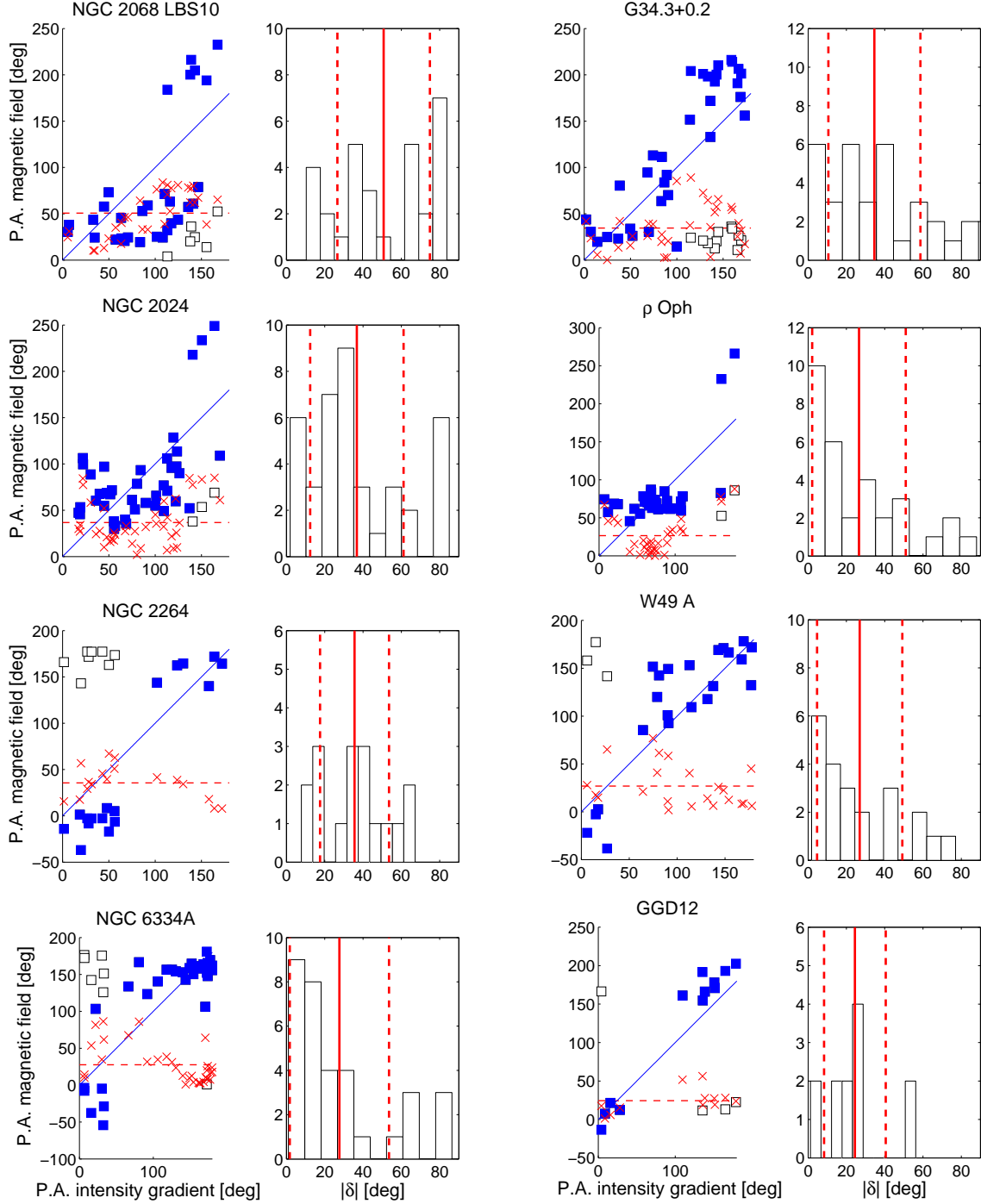


Fig. 21.— The correlation between the magnetic field and intensity gradient orientations together with the histogram for the absolute angle  $|\delta|$  in between the two orientations for the sources in the Figures 15 and 16.

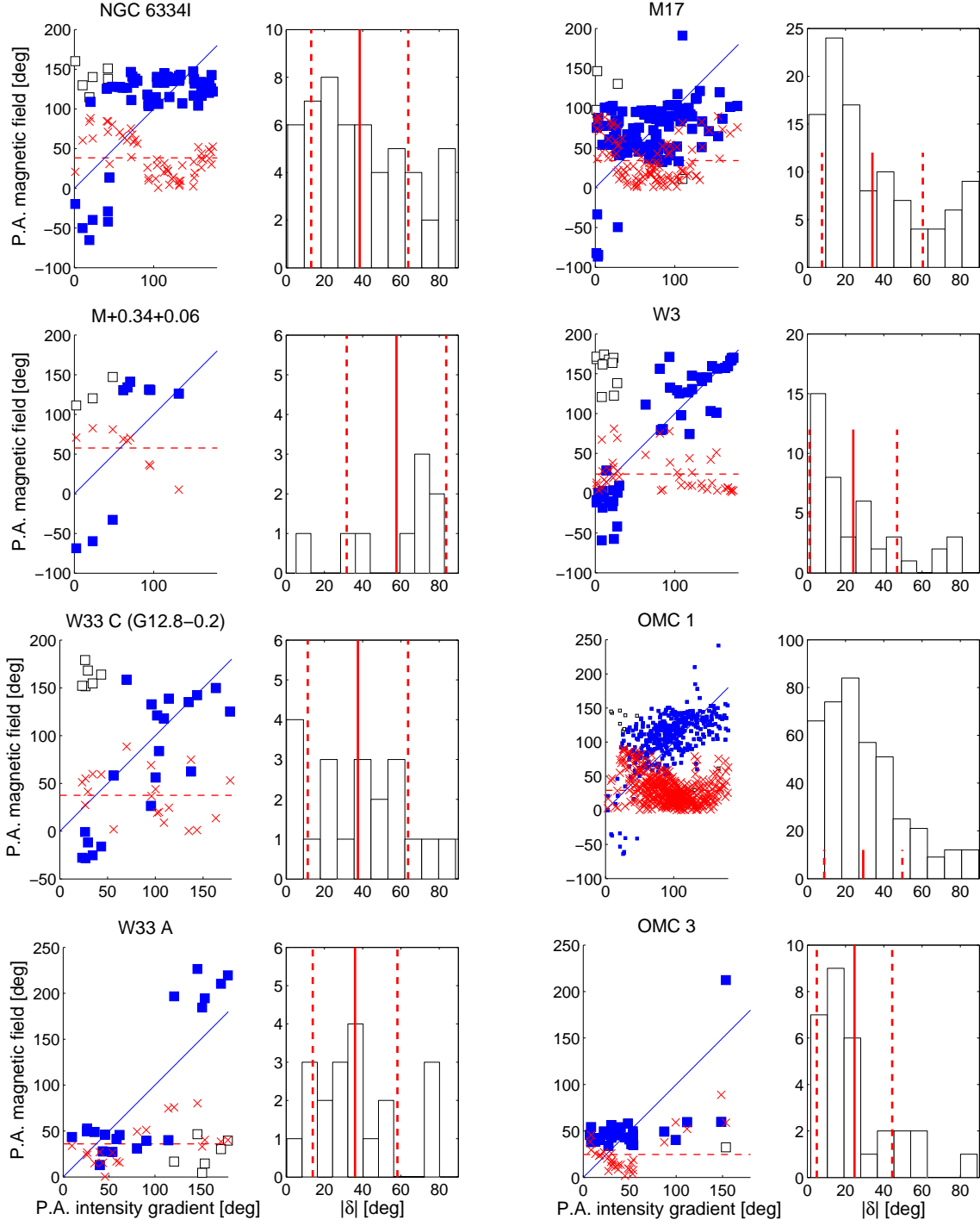


Fig. 22.— Same as in Figure 21 for the sources in the Figures 17 and 18.



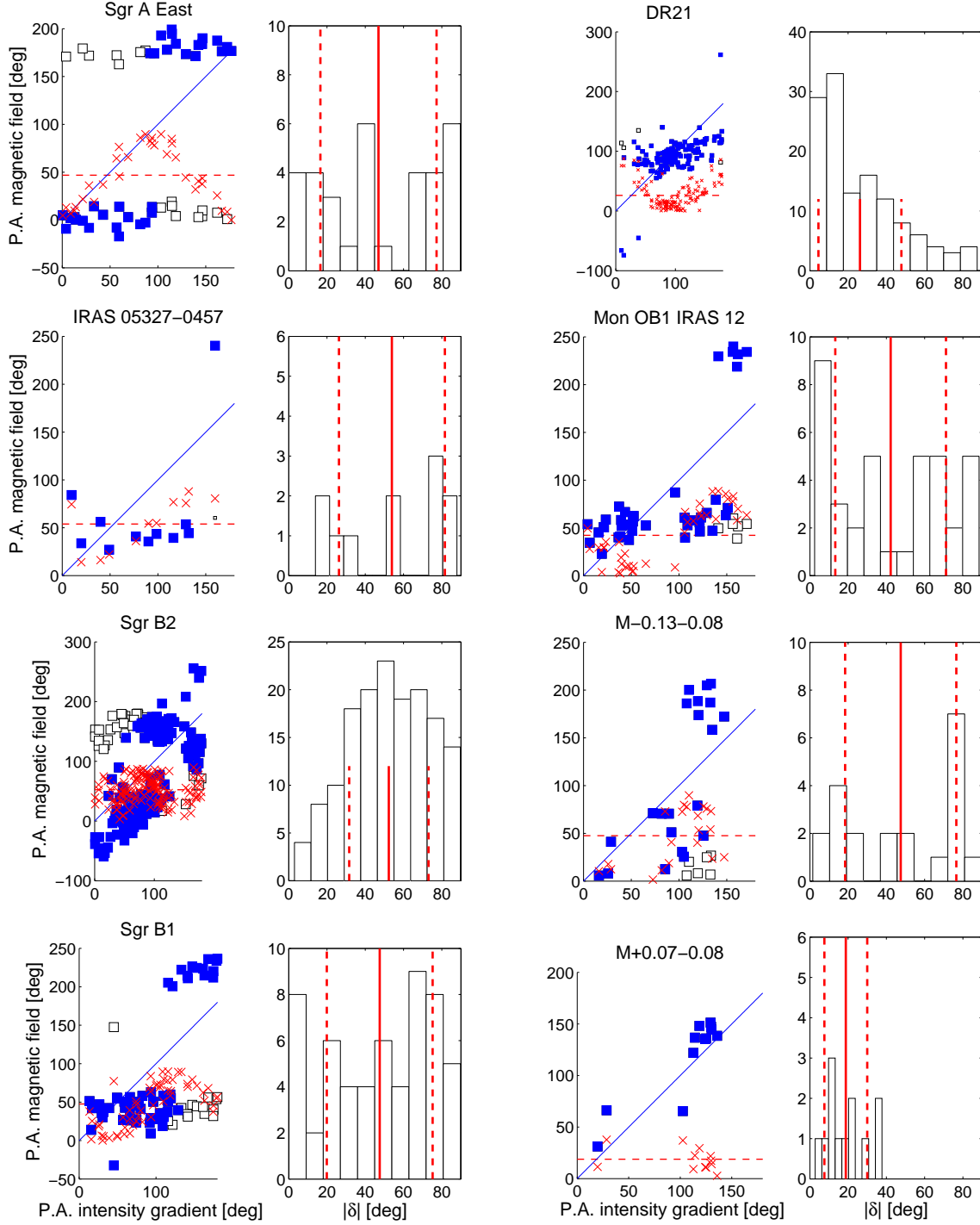


Fig. 23.— Same as in Figure 21 for the sources in the Figures 19 and 20.

Table 2. Analysis Summary

Observation					Analysis									Phase
Source / Region	$d$	$\lambda$	$\theta$	$\ell$	$\mathcal{C}$	$\delta_{max}$	$\delta_{min}$	$\langle  \delta  \rangle$	$std( \delta )$	$\Sigma_{B,max}$	$\Sigma_{B,min}$	$\langle \Sigma_B \rangle$	$std(\Sigma_B)$	
	(kpc)	( $\mu$ m)	( $''$ )	(mpc)		(deg)	(deg)	(deg)	(deg)					
	(1)	(2)	(3)	(4)	(5)	(6)	(7)	(8)	(9)	(10)	(11)	(12)	(13)	
CO+0.02/ M-0.02 <sup>a</sup>	7.9	350	20	770	0.71	90	-90	48	24	16.8	0.01	1.48	3.32	I
Mon R2	0.95	350	20	92	0.78	67	-55	23	18	1.56	0.09	0.57	0.35	IIA
M+0.25+0.01 <sup>a</sup>	7.9	350	20	770	0.61	88	-89	57	24	14.5	0.02	2.91	3.56	IIB
NGC 2068 LBS10	0.4	350	20	39	0.62	77	-84	51	24	5.02	0.002	1.38	1.42	IIB
NGC 2024	0.4	350	20	39	0.55	85	-85	37	24	7.14	0.02	1.03	1.17	IIA
NGC 2264	0.8	350	20	78	0.94	42	-67	36	18	1.66	0.04	0.63	0.51	IIB
NGC 6334A	1.7	350	20	170	0.84	86	-86	28	26	2.44	0.02	0.48	0.50	IIA
G34.3+0.2 <sup>a</sup>	3.7	350	20	360	0.87	89	-85	35	24	2.38	0.01	1.30	0.30	IIB
$\rho$ Oph	0.139	350	20	14	0.66	88	-78	27	24	5.90	0.09	0.93	1.00	IIA
W49 A	11.4	350	20	1110	0.55	77	-65	27	22	1.01	0.02	0.31	0.30	IIA
GGD12	1.7	350	20	170	0.98	56	-18	24	16	1.20	0.03	0.39	0.32	IIA
NGC 6334I	1.7	350	20	170	0.63	88	-84	38	25	5.76	0.01	0.96	0.91	IIA
M+0.34+0.06	8	350	20	780	0.81	71	-83	58	26	6.19	0.55	1.96	1.81	IIB
W33 C	2.4	350	20	230	0.80	89	-75	37	26	6.52	0.05	0.80	1.48	IIA / IIB
W33 A	2.4	350	20	230	0.87	80	-75	36	22	2.57	0.07	0.66	0.74	IIA
M 17 <sup>a</sup>	1.6	350	20	160	0.44	88	-90	34	26	4.46	0.02	0.78	1.05	IIA
W3	1.95	350	20	190	0.91	78	-81	24	23	5.83	0.04	0.70	0.96	IIA
OMC 1 <sup>a</sup>	0.414	350	20	40	0.59	86	-90	29	20	18.0	0.004	0.87	2.50	IIA
OMC 3 <sup>a</sup>	0.414	350	20	40	0.59	59	-89	25	20	1.61	0.02	0.88	0.65	IIA
Sgr A* East <sup>a</sup>	8	350	20	780	0.83	90	-90	47	30	8.00	0.13	2.20	3.00	I
IRAS 05327	0.414	350	20	40	0.43	81	-88	54	28	12.0	0.39	2.13	3.39	IIB
Sgr B2 <sup>a</sup>	8	350	20	780	0.70	90	-87	52	21	15.0	0.002	1.45	1.80	IIB
Sgr B1 <sup>a</sup>	8	350	20	780	0.76	90	-90	48	28	9.30	0.03	1.43	1.75	I / IIA
DR21	3	350	20	290	0.58	86	-87	26	22	4.38	0.00	0.75	0.59	IIA
Mon OB1 IRAS 12 <sup>a</sup>	0.80	350	20	78	0.65	88	-88	42	29	6.13	0.005	1.10	2.39	IIB

Table 2—Continued

Observation					Analysis									Phase
Source / Region	$d$	$\lambda$	$\theta$	$\ell$	$\mathcal{C}$	$\delta_{max}$	$\delta_{min}$	$<  \delta  >$	$std( \delta )$	$\Sigma_{B,max}$	$\Sigma_{B,min}$	$< \Sigma_B >$	$std(\Sigma_B)$	
	(kpc)	( $\mu\text{m}$ )	( $''$ )	(mpc)		(deg)	(deg)	(deg)	(deg)					
	(1)	(2)	(3)	(4)	(5)	(6)	(7)	(8)	(9)	(10)	(11)	(12)	(13)	(14)
M−0.13−0.08 <sup>a</sup>	8	350	20	780	0.71	90	−80	47	29	3.70	0.02	1.13	1.60	IIB
M+0.07−0.08	8	350	20	780	0.89	37	−37	19	11	0.54	0.002	0.24	0.20	IIA
W51 e2	7	870	0.7	24	0.95	34	−48	18	12	1.28	0.002	0.22	0.30	III
W51 North	7	870	0.7	24	0.89	82	−81	34	23	4.59	0.07	0.86	0.78	III
Orion BN/KL <sup>a</sup>	0.48	870	2.8	6.4	0.70	89	−90	44	25	5.28	0.02	1.18	1.30	III
g5.89 <sup>a</sup>	2	870	2.4	23	0.72	76	−84	35	26	3.03	0.07	0.79	1.20	-

Note. — Statistical quantities are based on the Figures 2, 3 and 4, and Figures 15 to 23. For sources with an upper index 'a', large outliers are removed in order to calculate  $\Sigma_{B,max}$ ,  $\langle \Sigma_B \rangle$  and  $std(\Sigma_B)$ .

<sup>(1)</sup>Source distance. Values are from Genzel et al. (1981) for W51 and Orion BN/KL, Acord et al. (1998) for g5.89, Racine & van de Bergh (1970) for Mon R2 and from Reid et al. (2009) for CO+0.02−0.02 / M−0.02−0.07 and M+0.25+0.01. For the sources in Appendix B: NGC 2068 LBS10 and NGC 2024 (Anthony-Twarog 1982), NGC 2264 (Park & Sung 2002), NGC 6334A and 6334I (Russek et al. 2012), G34.3+0.2 (Kuchar & Bania 1994),  $\rho$  Oph (Mamajek 2008), W49 A (Gwinn et al. 1992), GGD12 (Rodriguez et al. 1980), sources around the galactic center, i.e., M+0.34+0.06, Sgr A\* East, Sgr B2, Sgr B1, M−0.13−0.08, M+0.07−0.08 (Genzel et al. 2000), W33 C and W33 A (Immer et al. 2013), M17 (Povich et al. 2007), W3 (Xu et al. 2006), OMC 1, OMC 3 and IRAS 05327 (Menten et al. 2007), DR21 (Campbell et al. 1982), Mon OB1 IRAS 12 (Walker 1956).

<sup>(2)</sup>Observing wavelength.

<sup>(3)</sup>Beam resolution. For elliptical beams (synthesized beams of the SMA) the geometrical mean is adopted. For Hertz/CSO, the nominal beam size of  $\sim 20''$  is listed.

<sup>(4)</sup>Physical size scales at the source distances for the resolutions  $\theta$ .

<sup>(5)</sup>Correlation coefficient in the definition of Pearson's linear correlation coefficient between magnetic field  $P.A.s$  and the intensity gradient  $P.A.s$ .

- <sup>(6)</sup>Maximum difference between magnetic field and intensity gradient orientation.
- <sup>(7)</sup>Minimum difference between magnetic field and intensity gradient orientation.
- <sup>(8)</sup>Mean absolute difference between magnetic field and intensity gradient orientations.
- <sup>(9)</sup>Standard deviation of absolute differences.
- <sup>(10)</sup>Maximum magnetic field significance.
- <sup>(11)</sup>Minimum magnetic field significance.
- <sup>(12)</sup>Mean magnetic field significance.
- <sup>(13)</sup>Standard deviation of magnetic field significance.
- <sup>(14)</sup>Assigned phase (I, IIA, IIB, III) according to the schematic scenario in Figure 11. No phase is assigned to g5.89 because this source is probably in a later more evolved stage with expanding HII regions (Tang et al. 2009a).

Table 3. Evolutionary Sequence and Magnetic Field Features

Scale	Structure	$ \delta $ -patterns	$B$	Examples
large (I)	irregular	irregular	variable: minor, balanced, dominant	CO+0.02–0.02 / M–0.02–0.07
medium (IIA, IIB)	elongated	systematic	systematically varying with position	Mon R2, M+0.25+0.01
small (III)	symmetrized	systematic	systematic, increasingly radial	W51 e2, W51 North

Note. — Numbers in parentheses refer to phases in the schematic evolutionary scenario in Figure 11.